SANDIA REPORT

SAND2004-6683
Unlimited Release
Printed January 2005

Nanomaterials for Directed Energy Transfer

Steven C. Seel, Thomas A. Westrich, Jerrold A. Floro, Darryl Y. Sasaki, Julie A. Last
Andrea L. Slade, and Michael B. Sinclair

Prepared by
Sandia National Laboratories
Albuquerque, New Mexico 87185 and Livermore, California 94550

Sandia is a multiprogram laboratory operated by Sandia Corporation,
a Lockheed Martin Company, for the United States Department of Energy's
National Nuclear Security Administration under Contract DE-AC04-94AL85000.

Issued by Sandia National Laboratories, operated for the United States Department of Energy by Sandia Corporation.

Available to DOE and DOE contractors from
U.S. Department of Energy
Office of Scientific and Technical Information
P.O. Box 62
Oak Ridge, TN 37831

Telephone: (865)576-8401
Facsimile: (865)576-5728
E-Mail: reports@adonis.osti.gov
Online ordering: http://www.osti.gov/bridge

Available to the public from
U.S. Department of Commerce
National Technical Information Service
5285 Port Royal Rd
Springfield, VA 22161

Telephone: (800)553-6847
Facsimile: (703)605-6900
E-Mail: orders@ntis.fedworld.gov
Online order: http://www.ntis.gov/help/ordermethods.asp?loc=7-4-0#online

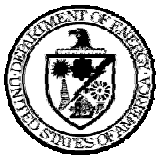

SAND 2004-6683
Unlimited Release
Printed January 2005

Nanomaterials for Directed Energy Transfer

Steven C. Seel, Thomas A. Westrich, and Jerrold A. Floro
Surface and Interface Sciences Department

Darryl Y. Sasaki. Julie A. Last, and Andrea L. Slade
Biomolecular Materials and Interfaces Department

Michael B. Sinclair
Microsystem Materials, Tribology, and Technology

Sandia National Laboratories
PO Box 5800
Albuquerque, New Mexico, 87185

Abstract

An extremely desirable functionality for nanostructured materials is the ability to efficiently activate or interrogate structures within a nanoscale device using optical energy. However, given the packing densities obtainable with nanofabrication, direct focusing of incident optical energy onto individual nanostructures is impractical. One approach to developing such functionality involves the use of "energy transfer". Energy transfer is the process by which excitation energy resulting from absorption of photons can become delocalized and move from the site where the photon was absorbed. Energy transfer is often associated with organized arrays, or networks, of polarizable structures. In the current context, energy transfer networks can loosely be thought of as "lenses" that "focus" optical energy onto a desired site. The research program described in this report investigated several approaches toward the fabrication of both organic and inorganic energy transfer networks. For the production of metallic nanoparticle chains and arrays which are expected to act as "plasmonic" waveguides, we investigated strain-induced self assembly of metal particles on insulating substrates. We found that up to 6 monolayers of Ag on MgO(001) produced self-assembled island structures, but that thicker films with larger island sizes no longer produced monomodal distributions or periodic ordering. Growth of metallic nanoparticles on templated MgO substrates was also investigated. In a separate endeavor, ultrathin amorphous Si and Ge films composed of nanoscale holes and islands on oxidized Si were discovered to exhibit anomalously low reflectivity over the visible spectrum. For a number of distinct material systems, the low reflectivity regime coincided with

the onset of percolation in the ultrathin films, suggesting that interparticle interactions and energy transfer might be playing a role. However, the optical behavior was successfully modeled using stratified medium theory, assuming homogeneous films, to predict reflectivity spectra and the thickness dependencies. Organic energy transfer networks were fabricated using two separate approaches. Langmuir–Blodgett techniques were used to prepare energy transporting J-Aggregates. These aggregates form upon compression of a 2-dimensional monolayer film of dye-derivatized amphiphilic molecules spread on a water surface. Fluorescence microscopy was used to monitor the size and shape of the aggregated domains. Characteristic changes in the molecular emission spectrum which occur upon aggregation, indicate the delocalization of excitation energy within the chromophore array. Finally, highly crystalline arrays of strongly interacting organic chromophores were synthesized. These crystals exhibit metallic-like reflectivity over a wide spectral band, indicative of strong coupling between the molecules in the array.

Contents

Figures

I. Introduction

An extremely desirable functionality for nanostructured materials is the ability to efficiently activate or interrogate structures within a nanoscale device using optical energy. However, given the packing densities obtainable with nanofabrication, direct focusing of incident optical energy onto individual nanostructures is impractical. The research program described in this proposal attempted to investigate how energy transfer phenomena can be harnessed to provide this functionality. Energy transfer is the process by which excitation energy resulting from absorption of photons can become delocalized and move from the site where the photon was absorbed. Energy transfer plays a prominent role in the photosynthetic process, where "light harvesting antennas" efficiently absorb sunlight and deliver the excitation energy to the photosynthetic reaction center. The antennas comprise arrays of absorbing organic chromophores that are coupled via near-field electromagnetic interactions. The coupling between the chromophores allows the excitation energy to hop from site to site, until it becomes trapped at a low energy site where it is utilized. In this context, energy transfer networks can loosely be thought of as "lenses" that "focus" optical energy onto a desired site. In addition to initiating chemical, structural or electrical processes, one can envision energy transfer networks that are used for efficient interrogation of the state of selected nanostructural units. In this case, absorbed optical energy is delivered to a fluorescent nanostructure whose emission properties depend upon the local state or environment.

This research program investigated the fabrication and optical behavior of organic and inorganic nano-arrays. Energy transporting arrays of organic chromophores, known as J-aggregates, were fabricated using Langmuir-Blodget techniques. These aggregates form upon compression of a 2-dimensional monolayer film of dye-derivatized amphiphilic molecules spread on a water surface. Fluorescence microscopy was used to monitor the size and shape of the aggregated domains. Characteristic changes in the molecular emission spectrum which occur upon aggregation, indicate the delocalization of excitation energy within the chromophore array. We have also demonstrated the ability transfer these aggregates to solid substrates for further investigation and/or integration with lithographically prepared structures. Highly crystalline arrays of strongly interacting organic chromophores were synthesized. These crystals exhibit metallic-like reflectivity over a wide spectral band, indicative of strong coupling between the molecules in the array. Propagation of electromagnetic energy in surface exciton modes, in a manner similar to the plasmonic energy transport predicted for metallic nanostructures, should be possible.

Metallic island formation and self-assembly during epitaxial deposition of Ag on MgO substrates was systematically explored. In general, we have found that the island size increases with deposition temperature. Through suitable choice of deposition temperature, rate, and thickness, we have prepared island arrays with average island sizes of 40 nm, and with narrow, monomodal size distributions. Over a range of deposition thicknesses, the island size remains the same, while the density of the islands increases with the total thickness of the deposition. Thus, we have been able to demonstrate experimental control over both the island size and spacing, both of which are critical for fabricating candidate plasmonic structures for optical characterization. We have also investigated methods to prepare terraced MgO substrates that can act as templates for the self-assembly of aligned nanoparticle chains. In particular, we have found that MgO annealed in O_2 at high temperature forms (110) facetted surfaces along steps created during cleaving.

In a separate endeavor, ultrathin amorphous Si and Ge films composed of nanoscale holes and islands on oxidized Si were discovered to exhibit anomalously low reflectivity over the visible spectrum. The optical behavior was successfully modeled using stratified medium theory, assuming homogeneous films, to predict reflectivity spectra and the thickness dependencies. The strong experimental correlation of low reflectivity observed near the percolation threshold coincides with the thickness of a homogeneous film that would produce a similarly low reflectivity. Based upon modeling predictions, the low reflectivity was a consequence of destructive interference within the multiple thin films and because of unexpectedly strong absorption by the amorphous films. Discontinuous polycrystalline Si, Ge, and Cu thin films with larger islands on oxide did not exhibit the same very low reflectivity. Thin film optical modeling including effective medium theory to account for the fractional substrate coverage were not able to capture the optical response and additional theory needs to pursued. The potential for the amorphous and discontinuous polycrystalline thin films as antireflection coatings is also discussed.

Each of these research avenues will be discussed more fully in the sections below.

II. Self-Assembled Growth of Ag on MgO

Background

The spontaneous formation of periodic nanostructures on crystal surfaces has been studied with increasing interest over the past decade.[1] One-dimensional structures such as periodically faceted surfaces and striped-planar domains can form, as well as two-dimensional ordered arrays of three-dimensional islands. Long range elastic interactions control this period ordering where elastic strain fields are created due to, for instance, lattice mismatch between deposited material and the substrate. Size uniformity can be thermodynamically controlled by a strain-induced equilibrium domain size. For example, self-assembly of islands in heteroepitaxial growth has been used to fabricate quantum dots with a specific size and narrow size distribution. For a system such as InAs quantum dots in GaAs matrix, the dot size must be within the range of 4-20 nm,[2] which is difficult to prepare by standard lithography techniques. Self-assembly of epitaxial metal islands, similar to our materials system of interest Ag/MgO, has been observed for Fe on NaCl.[3] In addition, our research group has experience using strain-mediated self-assembly to force ordered island heteroepitaxial growth in the Si_xGe_{1-x} on Si(001) system.[4]

The study of electronic transport and magnetic properties in nanowires and nanodot chains has been of growing interest due to the relentless drive to reduce device dimensions in microelectronics. Fabrication of these one-dimensional structures can be accomplished using templated substrates that have step edges created via cleaving, in the cases of NaCl and graphite,[5,6] as a result of polishing metal substrates,[7,8] or step-bunching on vicinal Si surfaces.[9,10] Selective growth of deposited material at step edges is traditionally called step decoration and can produce nanodots, and at larger thicknesses nanowires, with diameters equal to the step height. Growth at step edges is preferred because of low-energy attachment sites for nucleation and growth. In our application, we want to produce chains of metallic islands along step edges with heights in the 10's on nm range and believe that either strain-induced self-assembly and/or step decoration will generate size-selective growth of islands at step edges. If continuous nanowires form

along the step edges, a transformation back into the desired chain of islands may occur with high temperature annealing due to a Rayleigh instability.

Light can interact strongly with a single metal nanoparticle and excites a coherent collective electron motion, or plasmon. For a particle with a diameter less than the optical wavelength, the light-matter interaction leads to an oscillating polarization of the nanoparticle resulting in an oscillating dipole field. For a linear array of nanoparticles, the oscillating dipole induces a collective resonance that can propagate along the array communicating electromagnetic energy. The efficiency of the plasmon propagation relies on properly sized particles and particle spacings. Finite-difference time-domain simulations predict that a model plasmon waveguide made from Au would be composed of 50 nm diameter hemispheres with 75 nm center-to-center spacings.[11] Our goal is to produce similar linear island chains along steps edges in the Ag/MgO system.

MgO Preparation

Surface structure characterization of nominally [001]-oriented, vicinal-cut, and cleaved MgO(001) was performed to understand the effects of mechanical polishing, chemical etching, and O_2 annealing. The surfaces were examined mostly using atomic force microscopy (AFM) with occasional *in vacuo* reflected high energy electron diffraction (RHEED). The goals were to prepare large areas with atomically-flat surface and to create stepped surface with controllable terrace periodicity and step heights. For application in producing plasmonic waveguide structures, the steps would ideally be 50 nm in height and act as preferred growth sites for the metallic islands.

The as-received MgO(001) substrates (from Commercial Crystal Labs) had been mechanically polished to a nearly optically flat finish with an RMS roughness of approximately 30 ± 9 Å. The vicinal MgO(001) substrates were polished to 4° and 10° off-normal in a [100] direction. The surfaces were most likely amorphous due to damage from the mechanical polishing in agreement with diffuse RHEED patterns. The MgO substrates were ultrasonically cleaned for 10 min each in TCE, acetone, and methanol followed by drying with dry N_2. Samples were then chemically etched in concentrated phosphoric acid (H_3PO_4) for 30 s to remove the amorphous surface layer.[12] As shown in Fig 1, AFM revealed the anisotropic etching produces square features approximately 15 nm in height/depth and 250 nm in width, and increased the RMS roughness to about 75 Å. RHEED patterns of the etched MgO were sharper but with a diffuse background intensity. The vicinal-cut samples displayed similar surface morphologies as-received and after the H_3PO_4 etch.

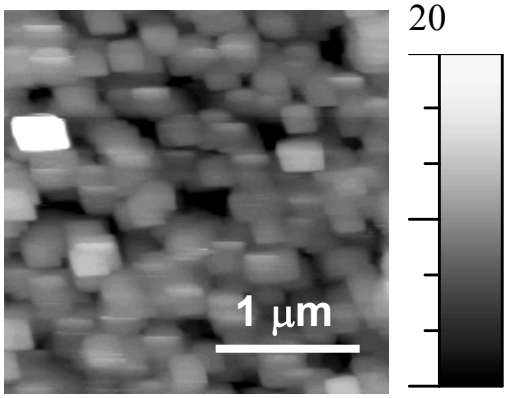

Fig .1. AFM of MgO(001) after 30 sec H_3PO_4 etch.

High temperature oxygen anneals of MgO(001) have been shown to result in well-ordered surfaces of atomically flat terraces with single and double step heights.[12,13] All of our O_2 anneals were performed in an alumina tube furnace for 2 hrs under an ultrahigh purity O_2 flow at 50 sccm/min. Anneals at 900°C produced only slight smoothening of the etch features and

resulted in increased pit formation for the vicinal-cut substrates. As shown in Fig. 2, anneals at 1000°C produced large pyramidal features for both the normal and vicinal MgO(001). In between the pyramidal structures a bumpy surface exist with an RMS roughness of about 8 Å. From the AFM it is not possible to resolve if these features are the result of step bunching. Longer H_3PO_4 etches, anneals at 1100°C, and longer anneals at 1000°C produced similar results. The reason for the discrepancy between our results using polished MgO substrates and those found in the literature is unknown.

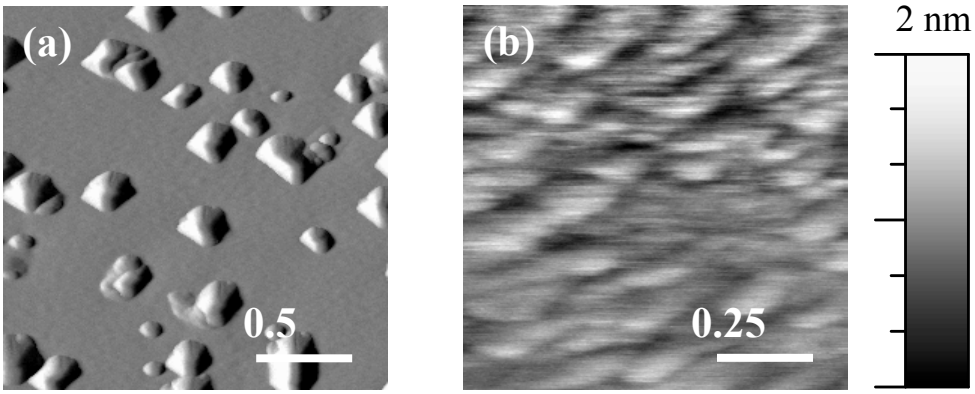

Fig. 2. AFM images of MgO after O_2 anneal at 1000°C (a) error signal (b) topograph of regions between pyramidal structures. Similar surface structures were observed for normal and vicinal MgO(001).

The original goal of annealing the miscut MgO substrates was to produce periodic terraces with controllable step heights. Since the O_2 anneals of the polished MgO samples did not work well, we examined surfaces created by cleaving MgO followed by high temperature O_2 anneals. As shown in Fig. 3, cleaving MgO generates (001) surfaces with many large cleavage steps of heights from 25 to 150 nm. The cleavage steps are not crystallographically aligned but instead the step orientation seems to be dictated by the direction that fracture propagates when the crystal is cleaved with a razor. Close inspection of an individual step in Fig. 3b shows a very irregular fracture surfaces. The cleaved MgO was then annealed for 2 hrs under an ultrahigh purity O_2 flow at 50 sccm/min. As shown in Fig. 4, the O_2 anneal results in faceting along [110] directions and faceted kinks along the length of the cleavage steps. The large steps in Fig. 4a are approximately 20 nm in height and the small steps in Fig. 4b range from 1–10 single step heights.

The faceting kinks in the cleavage steps may act as low-energy attachment sites during deposition and result in the formation of a chain of metal islands. If the in-plane orientation of the cleavage steps could be controlled, then it may be possible to control the periodicity of the faceted kinks produced by the O_2 anneal. Unfortunately, cleaving MgO produces uncontrollable step directions so we attempted to artificially create steps with varying in-plane orientation by focused ion beam (FIB) milling, as shown in Fig. 5a. From the surface profile shown in Fig. 5c, the walls of the trenches are not vertical but slope from the top to bottom. The FIB used in this study was an older model with a beam width near 1 μm which resulted in poor milling resolution. As shown in Fig. 6, a 1000°C O_2 anneal did not result in sharp steps with well-defined, evenly-spaced kinks as desired. An FIB with better milling capability would have been useful and this technique may still have merit in the future for creating templated substrates.

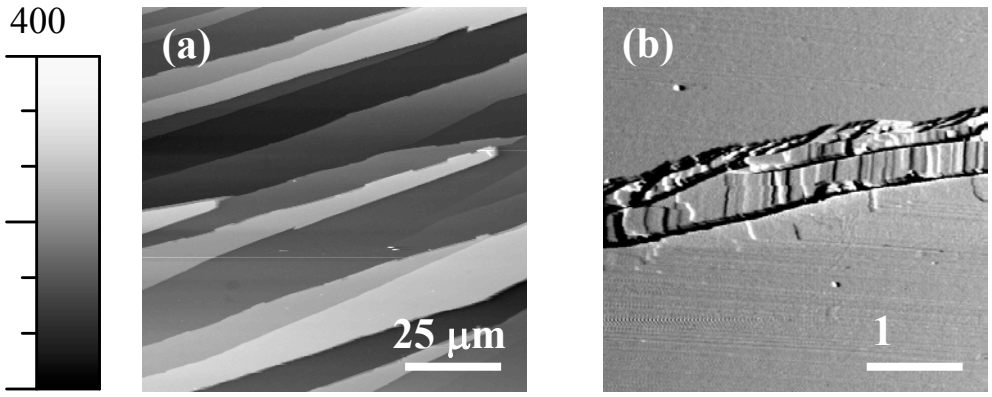

Fig. 3. AFM images of cleaved surface of MgO (a) topograph of large area (b) error signal of an individual step. The large cleavage steps are between 25 and 150 nm in height.

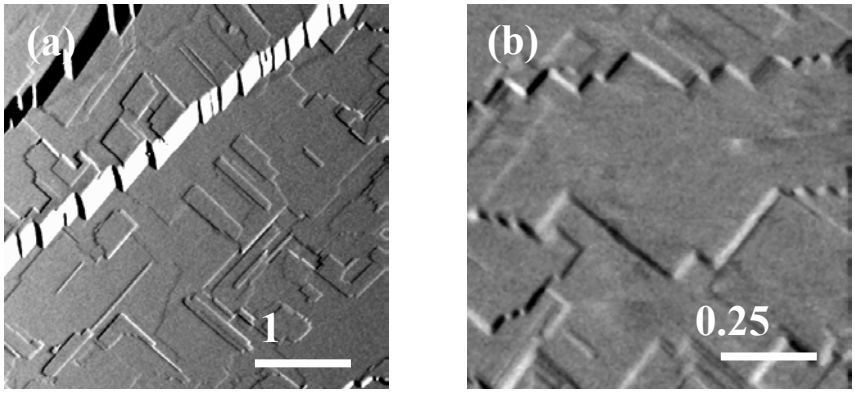

Fig. 4. Error signal AFM images of cleaved MgO after O_2 anneal at 1000^{o}C showing (a) large 20 nm steps with faceted kinks, and (b) flat region with small steps of 1–10 single step heights.

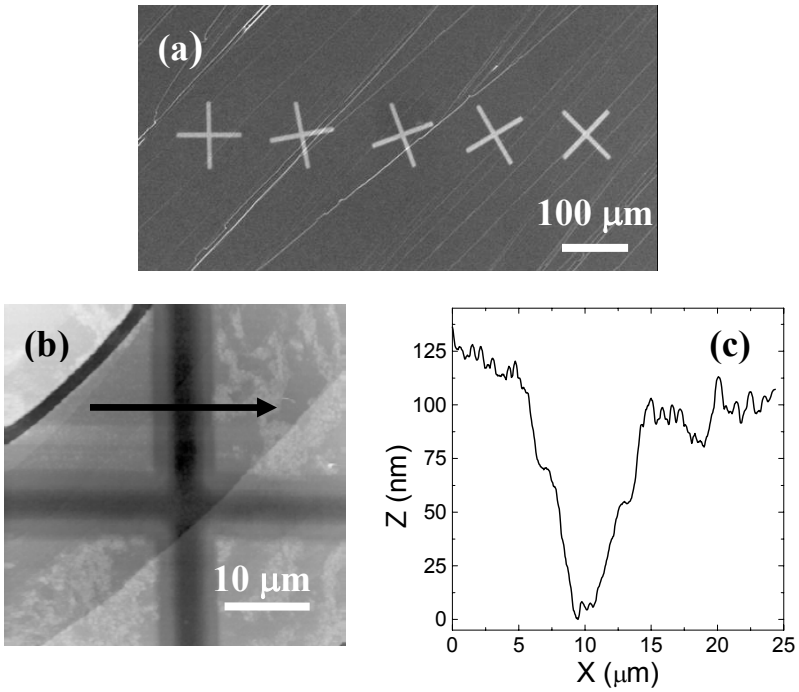

Fig. 5. FIB milled trenches (10-μm wide, 100-nm deep) in the surface of cleaved MgO (a) 50X optical image showing different orientations, (b) AFM of single trench cross, and (c) profile across trench.

Ag growth on MgO

The MgO substrates chosen for the metal epitaxy study were prepared by cleaving then annealing for 2 hrs under an ultrahigh purity O_2 flow at 50 sccm/min, resulting in surface similar to Fig 4. If the annealed MgO samples were not used immediately, they were stored in a desiccator to prevent hydroxide formation resulting from exposure to humidity.[14] After loading the MgO substrate in the vacuum chamber, the sample was outgased by slowly ramping the heater overnight to 400°C. In the morning with the sample at temperature, the base pressure in the chamber was typically below 2 x 10^{-9} Torr. The Ag films were deposited at 0.1 Å/min at normal incidence to the substrate by electron beam evaporation or from an effusion cell. The pressure during e-beam deposition was 1–2 x 10^{-7} Torr and 5–7 x 10^{-9} Torr for deposition from the effusion cell. For some runs, a scan shutter was used during deposition to create a series of thin film thicknesses across the sample. RHEED was available on the vacuum chamber but little information was gained from the very diffuse patterns obtained due to undiagnosed issues with the instrument. The Ag/MgO samples were analyzed using AFM and SEM, with additional X-ray texture analysis and Kikuchi back-scattered electron orientation mapping performed on select samples.

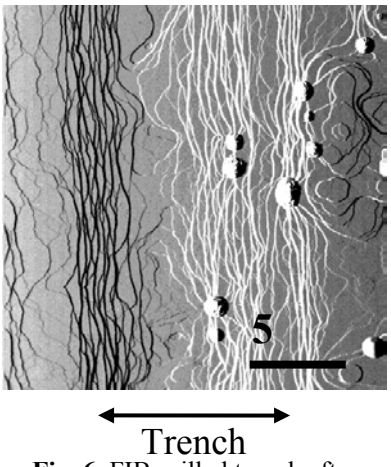

Fig. 6. FIB-milled trench after 1000°C O_2 anneal.

The deposition pressure in the 10^{-7} Torr range for operation of the e-beam system is higher than desirable for epitaxial growth. At that pressure, the time to form an adsorbed

monolayer of gas is only 10 secs, during which time ony an Å of Ag would have been deposited. The e-gun manufactured by MDC Vacuum had problems throughout this study due to leaks in the bellows of the rotating crucible and outgasing of the Kapton film used to reduce wear of the bellows. Unfortunately, these problems were never resolved since the deposition pressure for an e-gun system with our vacuum pumping capacity should run in the 10^{-9} Torr range.

Ag was chosen as the model material for growth on MgO(001) because of the known cube-on-cube epitaxial relationship, relatively low 3.0% lattice mismatch (a_{Ag}= 4.0853 Å, a_{MgO}= 4.2119 Å), and negligible chemical contributions to bonding. For nominally 2 monolayers (ML) of deposited Ag on MgO, changing the deposition temperature from RT to 100°C and up to 200°C increased the average island diameter (height) from 27 nm (2.0 nm) to 35 nm (3.0 nm) and up to 40 nm (6.5 nm), respectively. The RT and 100°C samples showed no obvious periodic ordering of the Ag islands, while the sample at 200°C showed signs of size selection and self assembly. To confirm ordering at 200°C, Ag films were grown on MgO with thicknesses of 2, 4, and 6 ML as shown in Fig. 7. The average island diameter (height) is 40 nm (6.5 nm) and is statistically similar for all three thicknesses. Notice that the island size distribution is monomodal with a relatively small standard deviation. Unfortunately as mentioned previously, the RHEED equipment on the vacuum chamber was not providing clear patterns and could not be used to confirm epitaxially growth of the Ag.

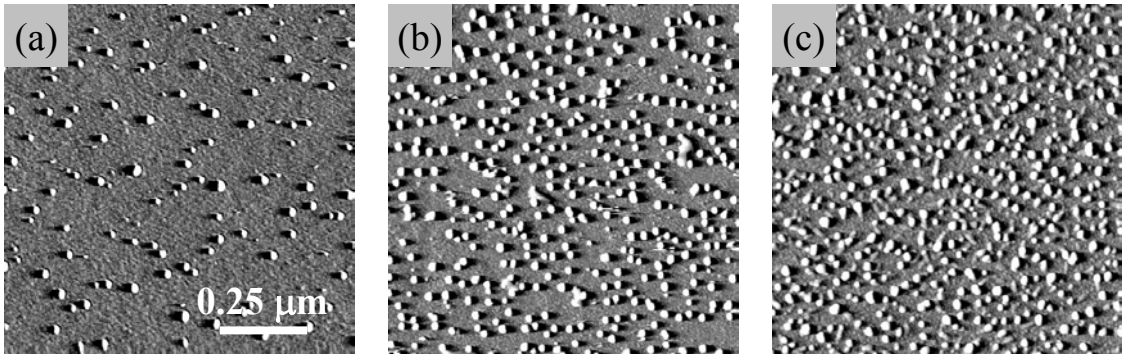

Fig. 7. Error signal AFM images of Ag films grown on MgO substrates at 200°C with film thickness of (a) 2 ML, (b) 4 ML, and (c) 6 ML. The average island diameter (height) is 40 nm (6.5 nm) and statistically similar for all three thicknesses.

Because larger Ag islands were desired for the plasmonic wire application, thicker 25 ML (5 nm) Ag films was deposited at 200°C on MgO as shown in the SEM image in Fig. 8. The AFM at our disposal does not have a tapping mode that produces accurate images, but tapping-mode AFM images taken in the CSRL agree well with the SEM image. In contact-mode, the process of laterally scanning the AFM tip pushed the Ag islands out of the scan area, as evidenced by the decreasing number of islands in successive scans of the same area. The poor adhesion of the large Ag islands with the MgO may indicate that the Ag is not coherently epitaxial and that misfit dislocations allow for shear at the interface. Misfit dislocations are energetically favorable as the total strain energy rises with increasing larger island size. Also notice in Fig. 8 that the islands vary in size from 25 to over 100 nm and do not display any periodic ordering.

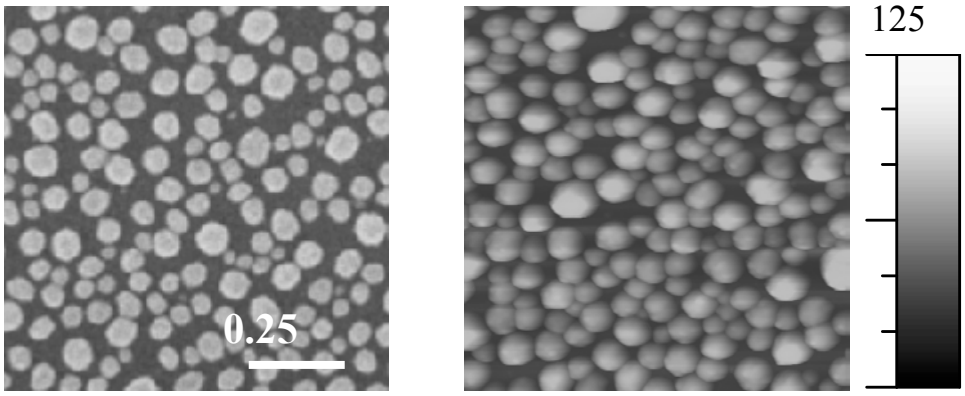

Fig. 8. 5 nm of Ag deposited at 200°C on MgO (a) SEM image, (b) tapping-mode AFM. The average height of the islands is approximately 50 nm.

The observation that the Ag island could easily be moved by the scanning AFM tip fostered the idea that linear chains of islands could be artificially created by manipulating the position of the islands. Unfortunately, our AFM does not have the capability to program discrete tip translations, but the idea presents an opportunity to create ordered Ag islands via a top-down approach at length scales unattainable by lithographic patterning.

The formation of Ag islands at cleavage steps was examined more carefully for different thicknesses and after high temperature anneals. For 5 nm of Ag deposited at 200°C, the islands formed randomly across the MgO surface without any preferential formation at the cleavage steps. Anneals at 400°C and 600°C for 2 hr in forming gas (97% Ar with 3% H_2) coarsened the islands leading to larger sizes but without segregation to cleavage steps. Increasing the Ag deposition thickness to 30 nm at 400°C resulted in continuous polycrystalline films with a cube-on-cube Ag/MgO orientation, as confirmed by x-ray pole figure and Kikuchi backscattered electron orientation mapping, but without any preference to growth at steps. For all deposition temperatures, film thicknesses, and annealing conditions examined, it was not possible to produced ordered Ag islands with the desired 50 nm size for study as plasmonic waveguides.

Subsequent investigation of the literature revealed that the three-dimensional growth of Ag islands on MgO(001) occurs coherently up to 4-6 monolayers before dislocations are introduced to relax the misfit strain.[15] Our results in Fig. 7 confirm that strain-induced self-assembly is observed for very thin Ag films, however for thicker Ag films the islands sizes are no longer monomodal and no ordering is observed, as shown in Fig. 8.

To increase the critical island size before creation of misfit dislocations, two different materials with similar/lower mismatch strains on MgO(001) were also studied. Fe and V have mismatch strains of 3.8% and 1.8%, respectively, on MgO(001) for [110]||[001] in-plane orientations. Unfortunately, no ordered island growth was observed for either material deposited over a range of thickness and deposition temperatures.

Conclusions and Future Work

The growth of Ag film on MgO(001) above 200°C resulted in self-assembled island structures for thicknesses up to 6 monolayers. Thicker films resulted in larger islands, which are desirable for the study of plasmonic waveguides, which were no longer size selective or periodically ordered. Different materials besides Ag with lower lattice misfits with the MgO, or

a different dielectric substrate, may allow for the formation of larger islands that remain coherent. Templated MgO substrates with step edges of appropriate ordering were created by cleaving and subsequent O_2 annealing. Unfortunately, the preferred growth of Ag islands along the step edges could not be achieved during growth or with subsequent heat treatment. Further study of the growth process is required to find the kinetic regime that leads to step decoration without island nucleation on the terraces. If that growth regime is discovered, then a more controlled step height and step kink density of the MgO substrate would be desirable for a more precisely templated surface. Our attempts to use focused ion beam (FIB) milling of the MgO were limited by the poor spatial resolution of the FIB at our disposal. Alternatively, the fabrication of a linear array of Ag islands may be possible using a top-down approach utilizing an AFM to manipulate the position of islands, as motivated by our difficulty in imaging Ag islands with poor adhesion with the MgO substrate.

III. Nanoscale Optical Materials

Background

The non-absorbing dielectric response of metals has recently been exploited for application in photonic materials.[16] The transmission of light through subwavelength hole arrays made in metal films can be orders of magnitude larger than expected from standard optical theory. The potential applications suggested for this transmission phenomenon include subwavelength photolithography, near-field microscopy, and wavelength-tunable filters.[17] The wavelengths at which the transmission peaks occur, and the fact that similar phenomena are not observed for dielectric films, suggests that surface plasmons in the metal are involved in the process.[18] The large electric field enhancements near the edges of the holes "sucks the light through the film" by trapping the surface modes as local plasmon resonances, which then propagate through the film and allow the light be re-transmitted.[16] Similar field enhancements have been long been applied in surface-enhanced Raman spectroscopy, where Raman signals from molecules on rough Ag surface may be enhanced by factors greater than 10^6.[19] Discontinuous metallic thin films deposited on a dielectric interlayer on a thick substrates also exhibit plasmon-resonance-dominated optical behavior.[20,21,22,23] Our investigation into the extremely low reflectivity of ultrathin semiconductor thin films, composed of an array of nanosized islands and holes, on oxidized Si substrates was motivated by the structure-property relationship observed for these discontinuous metal films. Our understanding of the origins of the low reflectivity and the connection with the discontinuous nature of the semiconductor films required a more systematic experimental and modeling investigation afforded by this LDRD project.

Discontinuous semiconductor film on oxidized Si

The motivation for this study on the optical properties of ultra-thin semiconductor film on oxidized Si was a consequence of a BES project examining the stress evolution during deposition. To measure thin film stress during deposition, a multiple-beam optical stress sensor (MOSS) monitors the deflection of a series of evenly-spaced laser beams reflected off the substrate surface onto which the film is being deposited.[24] Changes in the beam spacing are related to the substrate curvature resulting from the evolving stress in the deposited thin film. When Si or Ge films were deposited on oxidized Si substrates, the intensity of the reflected laser beam as detected by a CCD camera would effectively drop to zero over a limited range of film thicknesses. Upon visual inspection, the samples were deep blue in color indicating low reflectivity across most of the visual spectra. In this LDRD project, we more systematically examined the influence of semiconductor film thickness, film morphology, and oxide thickness on the reflectivity behavior. By varying the substrate temperature during deposition, the influence of the amorphous or crystalline nature of the film could also be examined. The reflectivity spectra of the samples were measured over the visible spectrum via specular and integrating sphere reflectometry. Classical thin film optics were used to model the semiconductor/oxide/Si system and compared to the measured spectra. Because of the extremely low reflectivity, their application as antireflection (AR) coatings was also considered in detail.

The MOSS measurements were taken during RT growth of amorphous Ge (aGe) at 0.5 Å/sec on a Si substrate with 700 Å of thermal oxide. Figure 9 shows the substrate curvature and reflected laser intensity versus film thickness (and vs. time once growth is stopped). Notice that the maximum substrate curvature (and therefore maximum tensile stress in the aGe film) approximately coincides with the minimum in the reflected laser intensity. For Volmer-Weber thin film growth, the onset of tensile stress generation (i.e., increasing positive curvature) is associated with island coalescence during deposition, and the maximum tensile stress coincides with the percolated film reaching continuity.[25,26,27] So from Fig. 9, the range of minimum reflectivity coincides with the thicknesses at which the film has a percolated island structure.

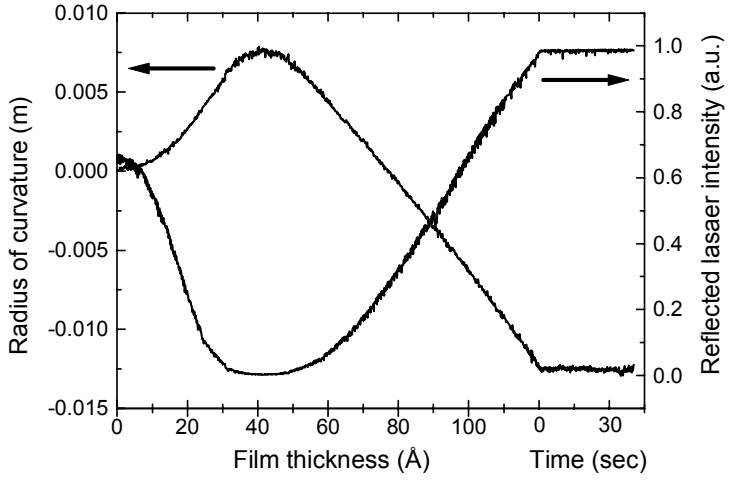

Fig. 9. *In situ* stress measurement of aGe during RT growth at 0.5 Å/sec on Si with a 700 Å oxide. The reflected laser intensity goes to zero over 30-50 Å.

Annular dark field transmission electron microscopy (ADF-TEM) of a 40Å-thick aGe film shown in Fig. 10 confirms the microstructural inference made from the curvature measurement. These images provide, to the best of our knowledge, the only known structural information related to the early stage of growth of aGe on oxidized Si. ADF microscopy is well suited to resolving the difficulty in achieving contrast between the amorphous Ge film and the underlying amorphous SiO_2 support.

A series of oxide thicknesses were created along the length of the oxidized Si substrates by pulling the substrate out of a buffered oxide etch (BOE) in discrete steps. The entire Si substrate was then cleaned in a piranha etch (3:1 sulfuric acid: hydrogen peroxide) for 15 mins to burn any organic compound contamination. After rinsing in DI water for 15 mins, the step-oxide Si substrate was viewed under a UV-inspection lamp before loading into the vacuum system. The sample was outgased under vacuum by slowly ramping the heater overnight to about 630°C, as confirmed by an optical pyrometer. In the morning with the sample at temperature, the base pressure in the chamber was typically in the low 10^{-10} Torr range. The sample was then flashed to 730°C for 5 mins and allowed to cool to the desired deposition temperature over 2 hrs. The Si and Ge thin films were deposited at 0.5 Å/sec at normal incidence to the substrate. A scan shutter was used during deposition to create a series of thin film thicknesses perpendicular to the steps in the oxide thickness.

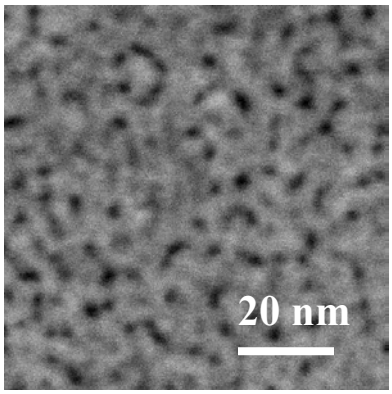

Fig. 10. Annular dark field TEM of 40 Å aGe deposited at RT at 0.5 Å/sec on oxidized Si.

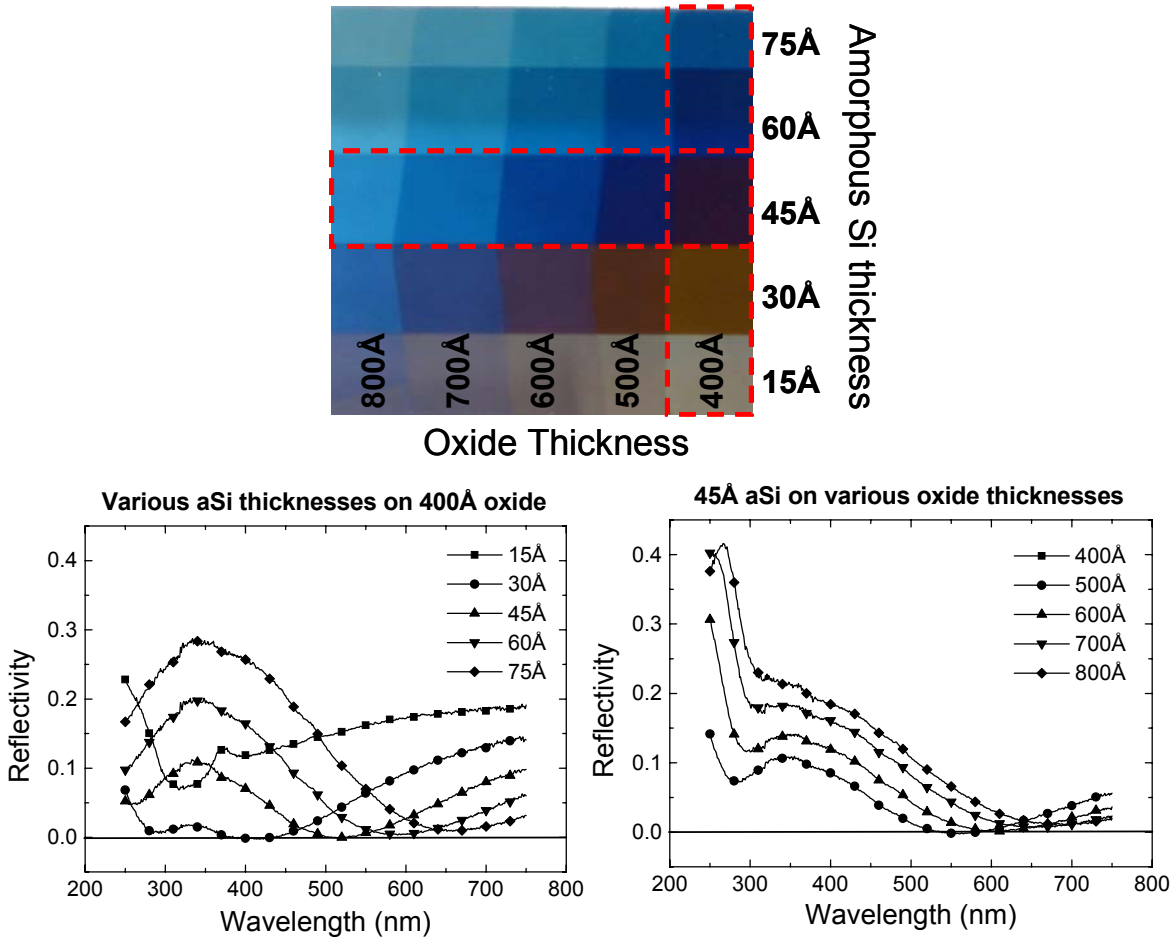

Fig. 11. Optical image (above) of a combinatorial sample with varying thickness of aSi deposited at RT at 0.5 Å/sec on various oxide thickness. The specular reflectivity spectra coincide with the highlighted row and column in the optical image.

As shown in Fig. 11, the combinatorial sample created by varying oxide and amorphous Si (aSi) thicknesses in perpendicular directions provides 25 different experiments from a single deposition. The aSi was deposited at RT and confirmed as amorphous by RHEED which showed diffuse diffraction rings. Also included in Fig. 11 are the specular reflectivity measurements made for varying thicknesses of aSi on 400 Å oxide, and for 45 Å aSi with various oxide thicknesses. Within this range of thicknesses, the wavelength at the minimum reflected intensity red-shifts with increasing aSi and oxide thicknesses. Figure 12 highlights a few reflectivity measurements from Fig. 11 along with calculated spectra from thin film optical modeling described later.

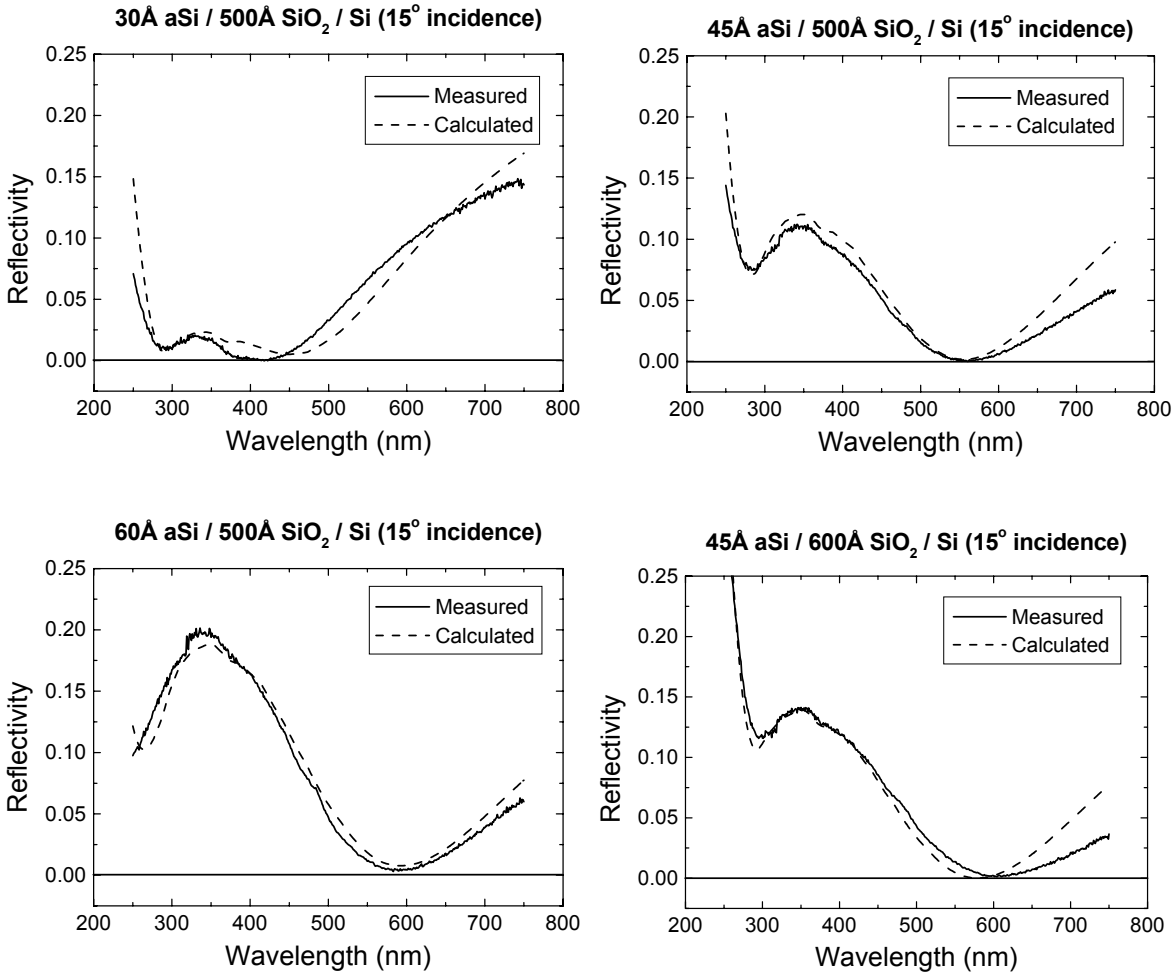

Fig 12. Specular reflectivity measurements for various aSi and oxide thickness for aSi deposited at RT at 0.5 Å/sec. The calculated curves are from thin film optical modeling assuming continuous, homogenous films.

The length scale of the structure created during deposition of the amorphous semiconductor films was assumed to be controllable by changing the deposition temperature. For metallic thin films deposited at temperatures at which some atomic mobility exists, decreasing the deposition rate and/or increasing the deposition temperature results in larger island sizes during Volmer-Weber growth.[28] However for aSi and aGe deposited up to 300°C

and for deposition rates varied over an order of magnitude, the microstructure through the final coalescence stage of growth was unchanged, as inferred from unchanging *in situ* stress measurements under various growth conditions. The extremely low mobility of aSi and aGe at these temperatures prevents any coarsening within the timescale of the deposition process. An interesting sidenote is the question of what determines the length scale of the holes and islands for aSi and aGe during growth if atomic mobility is effectively zero at low temperatures.

At even higher deposition temperatures, the microstructural length scale did increase but the semiconductor films become polycrystalline, as confirmed by RHEED. To avoid concerns of having a mixed amorphous/polycrystalline structure, the deposition temperature was generally made slightly higher than this transition temperature. Combinatorial experiments with varied thickness of Si (or Ge) and thermal oxide were performed at different deposition temperatures. Two sets of representative reflectivity measurements for polycrystalline Si (pSi) and polycrystalline Ge (pGe) films are shown in Fig. 13 along with SEM images of their microstructures. Also shown in Fig. 13, a spectrophotometer with an integrating sphere was used to measure reflectivity of the pGe sample and demonstrated that the low reflectivity is not related to significant light scattering by the islanded films.

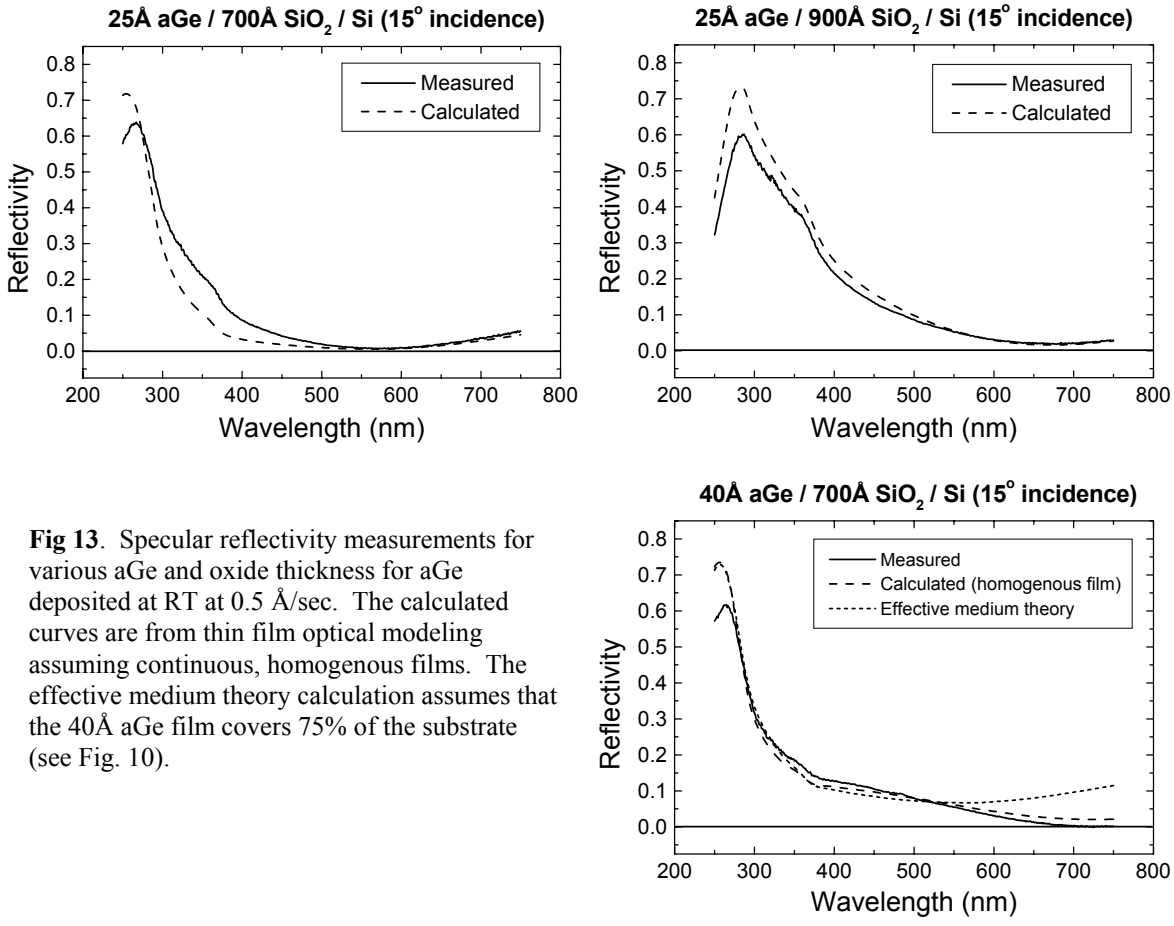

Fig 13. Specular reflectivity measurements for various aGe and oxide thickness for aGe deposited at RT at 0.5 Å/sec. The calculated curves are from thin film optical modeling assuming continuous, homogenous films. The effective medium theory calculation assumes that the 40Å aGe film covers 75% of the substrate (see Fig. 10).

In a separate vacuum system but under similar deposition conditions, Cu metal island films were grown on oxidized Si substrates. The reflectivity spectrum of the Cu sample along with an SEM of the microstructure is shown in Fig. 14. The Cu sample is similar to the semiconductor films in that the films are discontinuous but the optical response of the metal film is expected to be different because of the higher polarizability of Cu.

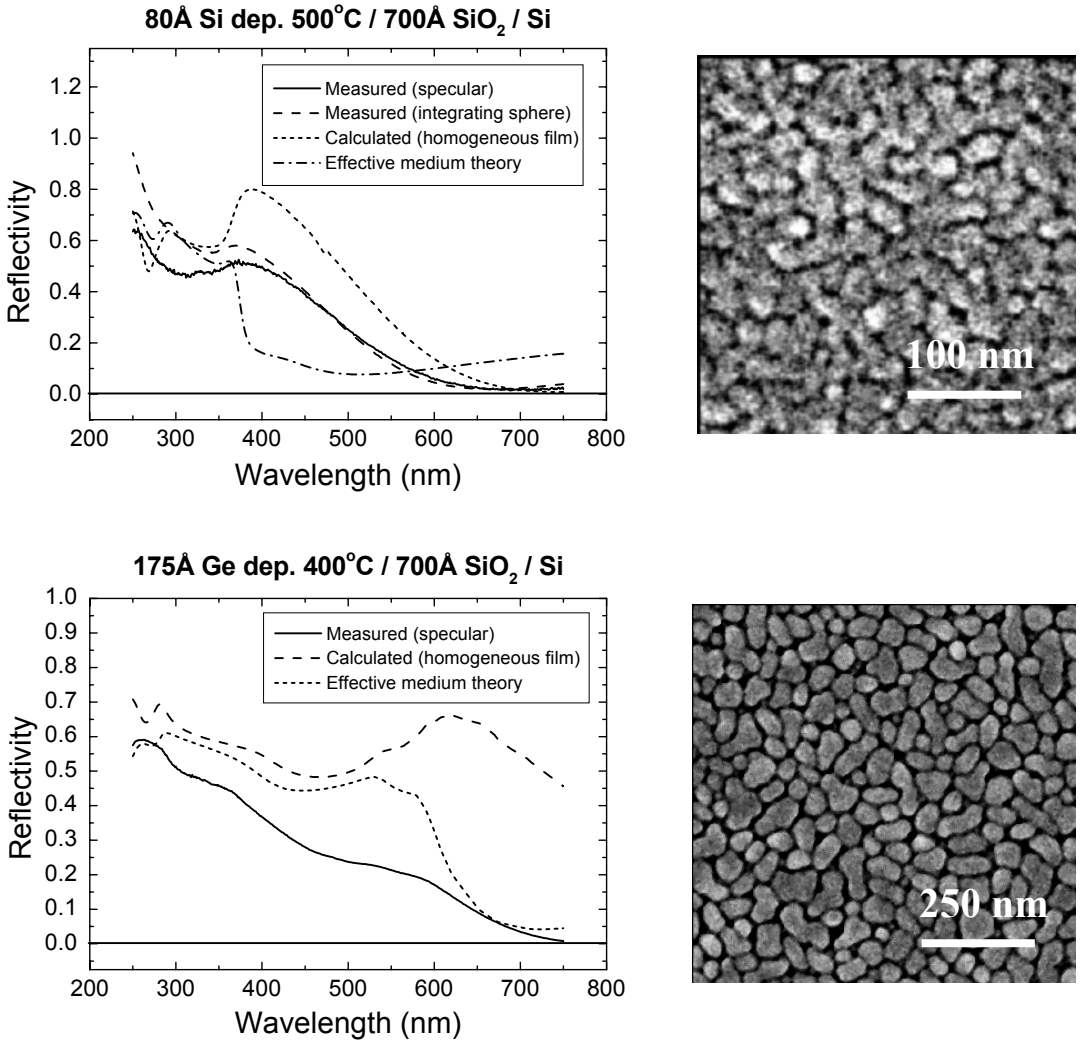

Fig 14. Reflectivity measurements for polycrystalline Si and Ge on 700Å oxide for films deposited at 0.5 Å/sec. The calculated curves are from thin film optical modeling assuming continuous, homogenous films. The effective medium theory calculation assumes 75% substrate coverage as estimated from the SEM images.

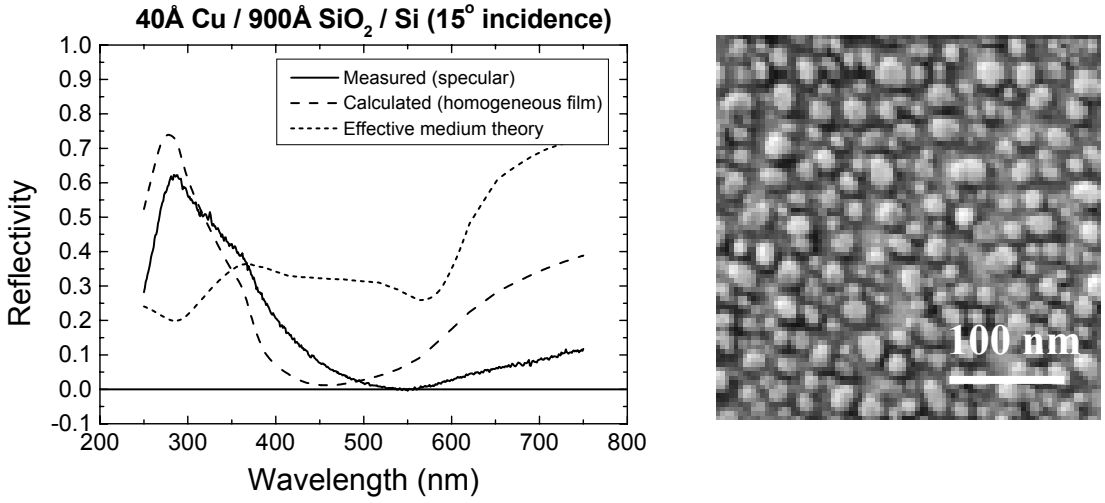

Fig. 15. Reflectivity measurements for polycrystalline Cu on 900Å oxide for films deposited at RT at 0.5 Å/sec. The calculated curves are from thin film optical modeling assuming continuous, homogenous films. The effective medium theory calculation assumes 60% substrate coverage as estimated from the SEM image.

Stratified Medium Optical Modeling

The optical response of the semiconductor thin films on oxidized Si system was modeling using a 4-layer stratified medium theory following the treatment by Born and Wolf.[29] A schematic of the primary light path through the multiple materials in the system is shown in Fig. 16. The indices of refraction for the semiconductor film and the Si substrate are complex (i.e., absorbing) and are given by $\hat{n} = n + ik$. The air and oxide are non-absorbing dielectrics and only have the real component of the index of refraction, *n*. From Snell's law of refraction:

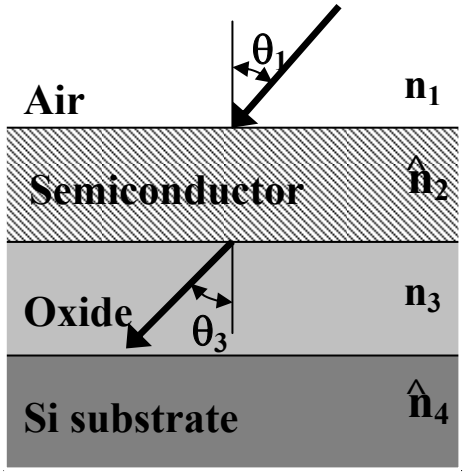

Fig. 16. Schematic of the 4-layer model used in the stratified medium optical modeling.

$$\sin\theta_j = \frac{n_1}{\hat{n}_j}\sin\theta_1, \qquad (1)$$

where the subscript *j* indicates the material layer indicated in Fig. 16, and so that $\sin\theta_2$ and $\sin\theta_4$ are complex functions, whereas $\sin\theta_1$ and $\sin\theta_3$ are real valued. For convenience later in the derivation, using the identity $\cos x = \sqrt{1-\sin^2 x}$ and inserting Eq. (1) yields:

$$\hat{n}_j \cos\theta_j = \sqrt{\hat{n}_j^2 - n_1^2 \sin^2\theta_1} = u_j + i\,v_j\,. \tag{2}$$

Equating the real and imaginary parts of Eq. (2) gives:

$$u_j = \frac{1}{\sqrt{2}}\left[\sqrt{\sqrt{\left(n_j^2 - k_j^2 - n_1^2\sin^2\theta_1\right)^2 + \left(2n_j k_j\right)^2} + \left(n_j^2 - k_j^2 - n_1^2\sin^2\theta_1\right)}\right], \tag{3a}$$

$$v_j = Sign(n_j k_j)\frac{1}{\sqrt{2}}\left[\sqrt{\sqrt{\left(n_j^2 - k_j^2 - n_1^2\sin^2\theta_1\right)^2 + \left(2n_j k_j\right)^2} - \left(n_j^2 - k_j^2 - n_1^2\sin^2\theta_1\right)}\right], \tag{3b}$$

where the sign of $n_j k_j$ determines the sign of v_j.. The roundtrip phase change through medium j is defined as:

$$\beta_j = \frac{2\pi}{\lambda_0} h_j \hat{n}_j \cos\theta_j = \eta_j\left(u_j + i\,v_j\right), \tag{4}$$

where λ_o is the wavelength of the incident light, h_j is the film thickness of material j, and $\eta_j = 2\pi h_j/\lambda_o$. Determining the real and imaginary components of trigonometric functions of complex functions will be useful later in the derivation:

$$\begin{aligned}\cos\beta_j &= u_{c,j} + i\,v_{c,j}\\ &= \frac{1}{2}\left[e^{i\beta_j} + e^{-i\beta_j}\right]\\ &= \frac{1}{2}\cos\left(\eta_j u_j\right)\left[e^{-\eta_j v_j} + e^{\eta_j v_j}\right] + i\frac{1}{2}\sin\left(\eta_j u_j\right)\left[e^{-\eta_j v_j} - e^{\eta_j v_j}\right],\end{aligned} \tag{5a}$$

$$\begin{aligned}\sin\beta_j &= u_{s,j} + i\,v_{s,j}\\ &= \frac{1}{2}\left[e^{i\beta_j} - e^{-i\beta_j}\right]\\ &= \frac{1}{2}\sin\left(\eta_j u_j\right)\left[e^{-\eta_j v_j} + e^{\eta_j v_j}\right] - i\frac{1}{2}\cos\left(\eta_j u_j\right)\left[e^{-\eta_j v_j} - e^{\eta_j v_j}\right].\end{aligned} \tag{5b}$$

For the electric vector perpendicular to the plane of incidence (TE wave), the reflection coefficient r_{TE} for a 4-layer stratified medium is given by:

$$r_{TE} = \frac{\left(m_{11} + m_{12}\hat{n}_4\cos\theta_4\right)n_1\cos\theta_1 - \left(m_{21} + m_{22}\hat{n}_4\cos\theta_4\right)}{\left(m_{11} + m_{12}\hat{n}_4\cos\theta_4\right)n_1\cos\theta_1 + \left(m_{21} + m_{22}\hat{n}_4\cos\theta_4\right)}, \tag{6}$$

where the matrix components m_{ij} are given by:

$$M = \begin{bmatrix} m_{11} & m_{12} \\ m_{21} & m_{22} \end{bmatrix} = M_2 \times M_3\,, \tag{7}$$

and

$$M_j = \begin{bmatrix} \cos\beta_j & \frac{-i}{\hat{n}_j \cos\beta_j}\sin\beta_j \\ -i\,\hat{n}_j \cos\beta_j \sin\beta_j & \cos\beta_j \end{bmatrix}, \qquad (8)$$

In terms of the reflection coefficient, the reflectivity is given by:

$$R = \left|r_{TE}\right|^2 . \qquad (9)$$

In the derivation above, all complex functions have been reduced to simple expression of the form $a + ib$ so that calculating the reflectivity is reduced to simple complex algebra.

It should be noted that all of our specular reflectivity measurements were performed at near-normal incidence (15^o) so that the reflectivity for the electric vector parallel to the plane of incidence (TM wave) is nearly identical to the TE wave reflectivity. However for completeness, the derivation of the reflection coefficient for the TM wave is exactly the same as for the TE wave, except that all occurrences of $\hat{n}_j \cos\theta_j$ are replaced by $\cos\theta_j / \hat{n}_j$. The overall reflectivity when considering both the TE and TM wave is then $R = 0.5(\left|r_{TE}\right|^2 + \left|r_{TM}\right|^2)$.

Comparison of model with measured reflectivity

The reflectivity spectra for aSi and aGe on oxidized Si were calculated using the stratified medium optics modeling described above. The indices of refraction for aSi, aGe, thermal oxide, and Si were taken from the literature.[30,31] Spectroscopic ellipsometry was performed to determine the optical properties of our aSi and aGe films as a function of wavelength and they agreed well with values in the literature, even though the deposition techniques and growth conditions were not identical.

As seen in Figs. 12 and 13, the calculated spectra for aSi and aGe on oxidized Si agree very well with the measured values for varying amorphous semiconductor and oxide thicknesses. The only calculated spectrum that does closely match the measured values is for the thinnest 30Å-thick aSi sample. One of the factors that has not been considered is the native oxide that forms on Si, but not Ge, during the time between removing the deposited sample from the vacuum chamber and measuring the reflectivity. A 12Å-thick native oxide on Si typically forms within a day of exposure to air at RT and consumes about 46% of the Si surface during oxidation (i.e. about 6 Å of Si). Additional thin film optics modeling of the 30Å-thick aSi sample was performed assuming a 12Å oxide/ 24Å aSi/ 500Å oxide/ Si substrate system. Including the native oxide improved the agreement between the calculated and measured curves in that the wavelength of the minimum reflectivity peak blue-shifted by 50 nm (not shown in Fig. 12). Similar calculations were performed for thicker aSi films and the importance of the native oxide on the reflectivity calculations becomes negligible.

The agreement between the calculated reflectivity and the measurements for the pSi and pGe samples, as shown in Fig. 14, is not as good as for the amorphous materials. The wavelengths associated with some of the minima/maxima are captured by the model, but overall the calculated reflectivity spectra do not model the optical response well.

Effective medium theory

As mentioned previously, the stratified medium theory assumes perfectly flat, homogeneous films whereas our films are composed of an array of island and holes, as shown in Fig. 10 for aGe and in Fig. 14 for pGe and pSi. Although limited TEM data has been collected for the amorphous films, stress measurements during deposition of aGe and aSi allow us to infer that the semiconductor thin films are not yet fully continuous.[27]

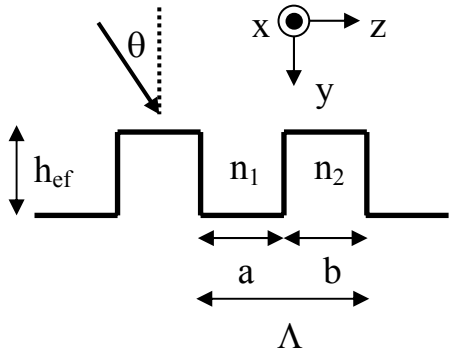

Fig 17. Grating configuration and notation for effective medium theory.

For an inhomogeneous material, an effective medium theory can be applied provided that the length scale of the structure Λ is subwavelength.[32] When $\Lambda \le \lambda/10$ the effective refractive indices for the TE wave, as a function of the fill factor $\sigma = b/\Lambda$ as defined in Fig. 17, becomes:

$$\hat{n}_{eff,TE} = \sqrt{\sigma \hat{n}_2^2 + (1-\sigma) n_1^2} = n_{eff,TE} + i\, k_{eff,TE}$$

$$n_{eff,TE} = \frac{1}{\sqrt{2}} \sqrt{\sqrt{\left[(1-\sigma) n_1^2 + \sigma\left(n_2^2 - k_2^2\right)\right]^2 + \left(2\sigma n_2 k_2\right)^2} + \left[(1-\sigma) n_1^2 + \sigma\left(n_2^2 - k_2^2\right)\right]}$$

$$k_{eff,TE} = \frac{1}{\sqrt{2}} \sqrt{\sqrt{\left[(1-\sigma) n_1^2 + \sigma\left(n_2^2 - k_2^2\right)\right]^2 + \left(2\sigma n_2 k_2\right)^2} - \left[(1-\sigma) n_1^2 + \sigma\left(n_2^2 - k_2^2\right)\right]} \qquad (10)$$

where $\hat{n}_2 = n_2 + i\, k_2$ and material 1 is this case is air. To conserve mass of the thin film, an effective film thickness must be defined equal to $h_{eff} = h/\chi$ and the fill factor $\sigma = \sqrt{\chi}$ where χ is the fractional substrate coverage as determined from microscopy.

Based up the TEM image shown in Fig. 10, the 40Å aGe film has a fractional substrate coverage $\chi = 0.75$ and an in-plane length scale of less than 10 nm, which satisfies the assumption that $\Lambda \le \lambda/10$. As can be seen in Fig. 13, the reflectivity spectrum for the 40Å aGe film calculated using the effective refractive indices does not agree with the measured data as well as that calculated assuming a homogeneous thin film. Unfortunately the TEM image does not give topological information and AFM could not resolve the features of the aGe film, so the actual structure is not well known and the assumption in the effective medium calculation may not be appropriate.

The indices of refraction of Eq. (10) resulting from effective medium theory are only valid when $\Lambda \le \lambda/10$. The microstructures of pSi and pGe films shown in Fig. 14 are larger than that limit, so more sophisticated models that account for the microstructural length scale are required. The effective refractive index of a grated region in the TE wave configuration with dimensions shown in Fig. 17 is given by:[33]

$$\cos(k_{1z} a)\cos(k_{2z} b) - \frac{1}{2}\left(\frac{k_{2z}}{k_{1z}} + \frac{k_{1z}}{k_{2z}}\right)\sin(k_{1z} a)\sin(k_{2z} b) = \cos(k_v n_1 \Lambda \sin\theta), \quad (11)$$

where $k_{1z} = \sqrt{n_1^2 k_v^2 - \beta_{TE}^2}$, $k_{2z} = \sqrt{n_2^2 k_v^2 - \beta_{TE}^2}$, and $k_v = 2\pi/\lambda_0$, and notice that β_{TE} must be solved for numerically. The effective index of refraction for the TE configuration is $n_{eff,TE} = \beta_{TE}/k_v$. Unfortunately, attempts to use the microstructure-based effective medium theory of Eq. (11) did not yield meaningful results when applied to absorbing materials like Si and Ge. Consequently, the simple effective medium model of Eq. (10) was used to model the pSi and pGe film assuming 75% substrate coverage for both. As shown in Fig. 14, the effective medium calculations of the pSi and pGe spectra are no better than those assuming a continuous, homogeneous film. More work is required to accurately account for the microstructure of pSi and pGe films in trying to model the reflectivity behavior.

Reflectivity-structure correlation

The correlation observed experimentally between the low reflectivity and the percolated structure of the amorphous semiconductor films is not supported by the success of the thin film optics modeling, which assume homogeneous films. As mentioned previously, laser-reflectivity-based stress measurements performed during growth provided reflected laser intensity at a wavelength of 635 nm as a function of an evolving film thickness (see Fig. 9). Thin film optics modeling was used to calculate reflectivity vs. film thickness at 635 nm to compare against the measured reflectivity for both aSi and aGe, as shown in Fig. 18. The *in situ* reflectivity measurement was made at a 40° angle of incidence so both the TE and TM wave was considered in the modeling. The relatively strong agreement between the measured and calculated curves in Fig. 18 seems to demonstrate that the low reflectivity observed near percolation is also the thickness at which multiple thin film destructive interference is strongest. In addition, the expectation that the discontinuous Si and Ge films would have a plasmon resonance effect was misguided because of their low polarizability due to a limited number of free carriers. Only the noble metals such as Au, Ag, and Cu with the highest polarizability are expected to have strong plasmon resonance response.

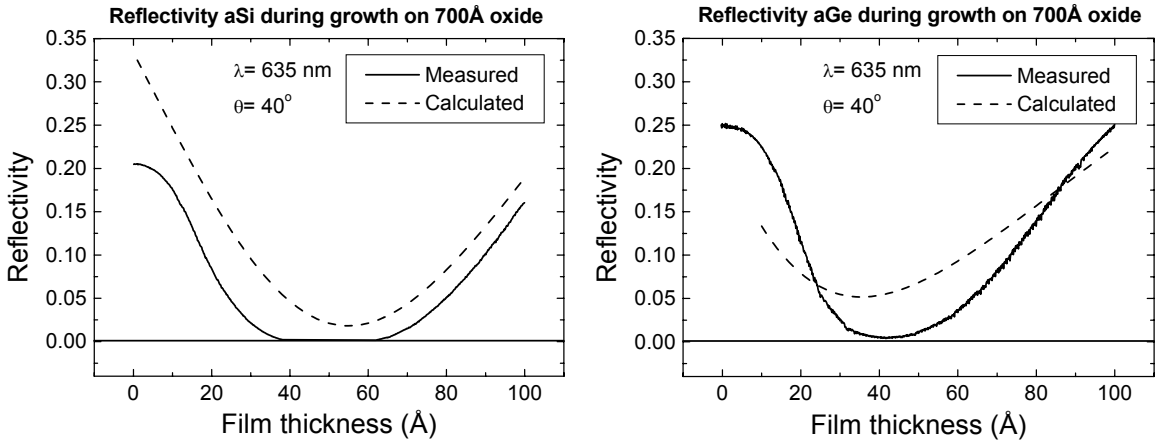

Fig. 18. Reflectivity as a function of film thickness during deposition of Si and Ge at RT. The curves in the plots allow comparison of measured reflectivity from MOSS using a 635 nm laser, and calculated values from thin film optical modeling.

Antireflection coatings

As shown in Fig. 19, bare Si has an average reflectivity over the visible spectrum of 45%, which is detrimental for applications such as photodetectors and photovoltaics that need to harvest light. Adding 500 Å of thermal oxide reduces the reflectivity to about 35%, but the additional of an additional 30 Å of aSi reduces the average reflectivity to less than 10%. Because of the very low reflectivity of these thin semiconductor films on oxidized Si, their use as anti-reflective (AR) coatings was investigated.

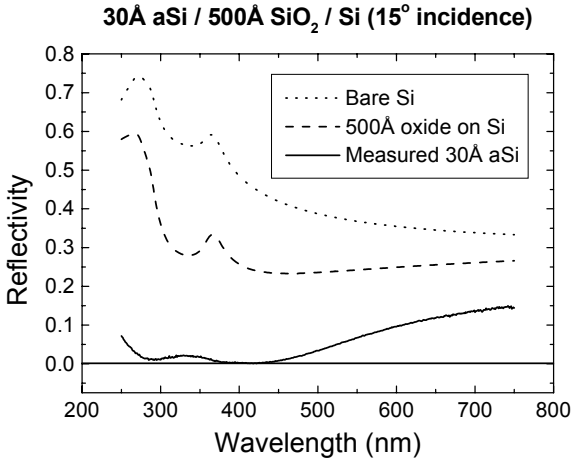

Fig 19. Reflectivity spectra for bare Si, Si with 500Å thermal oxide, and 30Å aSi / 500Å thermal oxide / Si.

The potential advantages of semiconductor AR coatings are the chemical and physical stability of the films (as compared to AR coatings based on metallic plasmonic films), the short deposition time during fabrication to deposit a few 10's of Å of material, and the compatibility with semiconductor processing as required for photodetector and photovoltaic devices. The other requirements for AR coatings are low broadband reflectivity and little to no absorption by the coating. The degree of absorption can be determined by a combination of reflectivity and transmission spectra, but a transmission measurement is our case not possible because of the thick Si substrate. Instead, the absorptivity can be determined through modeling based upon confidence from the excellent agreement of the calculated spectra with the measured reflectivity. In the simplest case, consider a freestanding 50 Å aSi film with air sandwiching the surfaces above and below. The reflectivity can be calculated using the formalism outline previously, and the transmission coefficient t and transmissivity T for an incident TE wave are given by:

$$t = \frac{2 n_1 \cos\theta_1}{(m_{11} + m_{12}\hat{n}_3 \cos\theta_3) n_1 \cos\theta_1 + (m_{21} + m_{22}\hat{n}_3 \cos\theta_3)}$$

$$T = \frac{n_3 \cos\theta_3}{n_1 \cos\theta_1} |t|^2$$

where materials 2 is the aSi, and materials 1 and 3 are air. The absorptivity A is then simply $A = 1 - R - T$. As shown in Fig. 20(a), the 50 Å aSi freestanding film absorbs almost 50% of the incident light at a wavelength of 300 nm. The low absorption at 750 nm occurs because the wavelength is nearing the band edge of aSi (~0.8 eV). The associated absorption coefficient of aSi at 300 nm is greater than 10^6 cm^{-1}, which is an order of magnitude greater than that of crystalline Si,[34] and explains why such a thin film can absorb so much of the incident light. The absorption by the 50 Å aSi film when on 500 Å oxide on Si is even greater, approaching 80% at a wavelength of 300 nm, as shown in Fig. 20(b). The absorption is enhanced compared to the freestanding film because of extra reflections off the SiO_2/Si interface that pass through the aSi

film again. While not promising for AR coatings, the enhanced absorption within an aSi thin film by creating a reflective backplane could be applied to amorphous thin film photovoltaics to increase their efficiency.

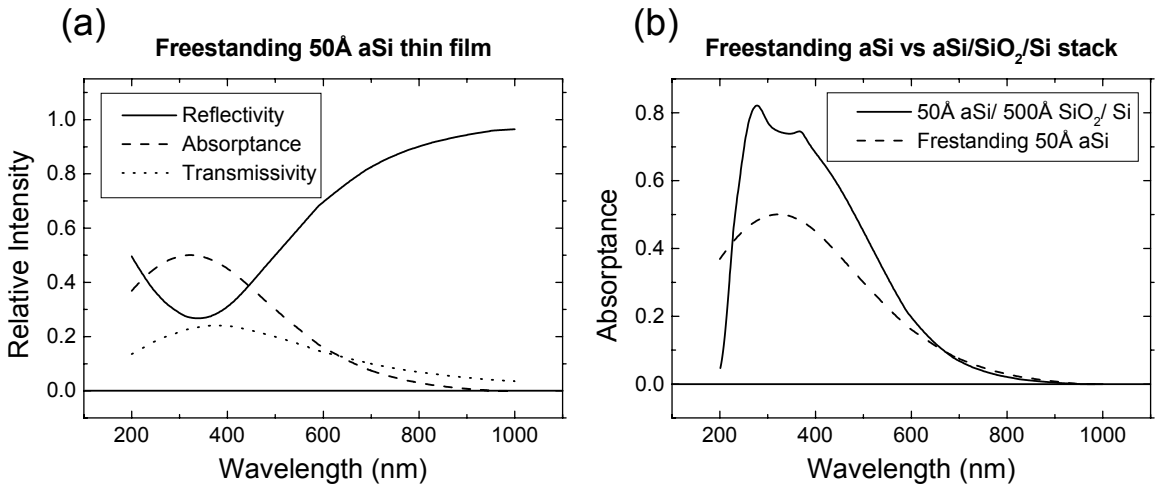

Fig 20. (a) Reflectivity, absorptance, and transmissivity of a freestanding 50Å-thick aSi film calculated using the thin film optics modeling, (b) Absorptance spectra for a freestanding 50Å-thick aSi film compared to the same film on an oxidized Si substrate.

While our calculations seem to indicate that the low reflectivity is partially a consequence of high absorption in the aSi and aGe samples, other research groups have used discontinuous metal island films, which are also absorbing, to enhance the efficiency of semiconductor photodetectors.[35,36] As shown in Fig. 15, we have observed low reflectivities in Cu on oxide that cannot be matched to by the stratified medium optical modeling, similar to the Si and Ge films shown in Fig. 14. The potential exists that the Si and Ge films on oxide may exhibit behavior similar to the metal island films. Further work would include measuring the efficiency of photodetectors or photovoltaics coated with and without discontinuous semiconductor films on oxide.

Conclusions and Future Work

Ultrathin amorphous Si and Ge films composed of nanoscale holes and islands on oxidized Si were found to exhibit anomalously low reflectivity over the visible spectrum. The reflectivity spectra of the amorphous film structures was successfully modeled using stratified medium theory, which assumes homogeneous films, including trends with varying semiconductor and oxide thicknesses. The strong correlation of low reflectivity observed near the percolation threshold for the amorphous film observed experimentally coincidences with the thickness of a homogeneous film that would produces a similarly low reflectivity, as predicted by our optical modeling. Based upon modeling predictions, the low reflectivity was due to the advantageous thicknesses of the multiple thin films resulting in antireflection characteristics, but also because of unexpectedly strong absorption by the amorphous films. Discontinuous polycrystalline Si, Ge, and Cu thin films on oxide with larger islands did not exhibit the same very low reflectivity. Thin film optical modeling including effective medium theory to account for the fractional substrate coverage were not able to capture the optical response and additional theory needs to pursued. The strong absorption by the amorphous films, as predicted by the optical modeling,

suggests that they would not be appropriate for antireflective coatings. However measurements of the efficiency of photodetectors or photovoltaics coated with and without discontinuous semiconductor films on oxide would provide invaluable insight, especially considering the optical modeling could not capture the behavior of the polycrystalline Si, Ge, and Cu films on oxide.

IV. Synthesis and Characterization of Carbocyanine Dye

Perhaps the ultimate degree of energy delocalization that can be achieved occurs within certain cyanine dye crystals. The crystalline arrangement of the chromophores causes the optical properties of these crystals to differ in remarkable ways from those of the individual, isolated molecules. In particular, because of the strength of the coupling between molecules, the wavepacket for a single exciton extends over a collection of neighboring molecules, greatly enhancing the strength of the lowest energy optical transition. This leads to a narrow, intense optical absorption spectrum, which, in turn, causes the real part of the dielectric constant to become negative for a substantial energy range (1.7 – 2.2 eV). The net result is the appearance of a "quasi-metallic" reflectivity band. Within this band, it is possible to propagate electromagnetic energy along the surface of the crystal in excitations known as exciton surface polaritons. Such excitations share many of the characteristics of the surface plasmons that occur on metallic nanoparticles, and thus, it might be possible to guide the flow of energy in a manner similar to what is now being pursued in the field of plasmonics. However, in the case of the organic crystals, we now have the opportunity to tailor the optical properties to achieve larger propagation distances than are achievable with plasmons.

Carbocyanine dyes are well known as excellent chromophores for photographic film and optical recording media.[37] Part of their unique properties is their wide range of photonic behavior in aggregate and crystalline form that leads to a broad spectrum of colors, photoluminescence, and non-linear optical properties. Modifications of the dye structure could yield new aggregated, or supramolecular, and crystalline structures offering novel and desirable optical characteristics for energy transfer schemes.[38]

Our initial efforts in this area to produce novel carbocyanine dye structures took on the synthesis of the cyclopropyl derivative **1**. The synthesis of this dye was accomplished through the multistep procedure illustrated in Figure 21.[39,40] In the first step, cyclopropylcarboxaldehyde was coupled with methoxymethyltriphenylphosphonium chloride to yield E- and Z-isomers of 1-cyclopropyl-2-methoxyethylene via the Wittig reaction. To this compound was reacted the Vilsmeier reagent in methylene chloride with K_2CO_3, followed by hydrolysis to yield cyclopropylmalonate. Coupling of this compound with tetramethylindolium iodide and acetic anhydride at high temperature gave the iodide version of the desired carbocyanine dye. Further purification through an ion pairing chromatography column followed by ion exchange with tetrafluoroborate and repeated recrystalization in isopropanol gave the desired compound as a dark purple solid.

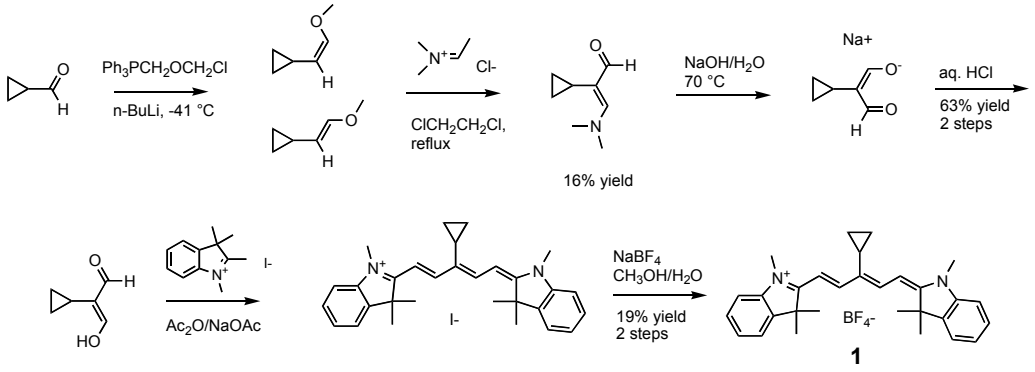

Figure 21. Synthesis of cycloproplyl carbocyanine dye.

Large crystals of the dye molecule were prepared by recrystallization in methanol with slow cooling. The hot recrystallizing solution flask was first placed in a 60 °C water bath held in a Dewar and the system sealed and allowed to cool to room temperature over a period of a day. The flask was then chilled to –10 °C in a freezer over night. Crystals were collected, washed with isopropanol, and dried under vacuum at ambient temperature. The crystals have a blue metallic luster over the surface. Pictures of the 2 – 3 mm size crystals are shown in Figure 22. An X-ray crystal structure of the compound was obtained to confirm structure and counterion (Figure 3).

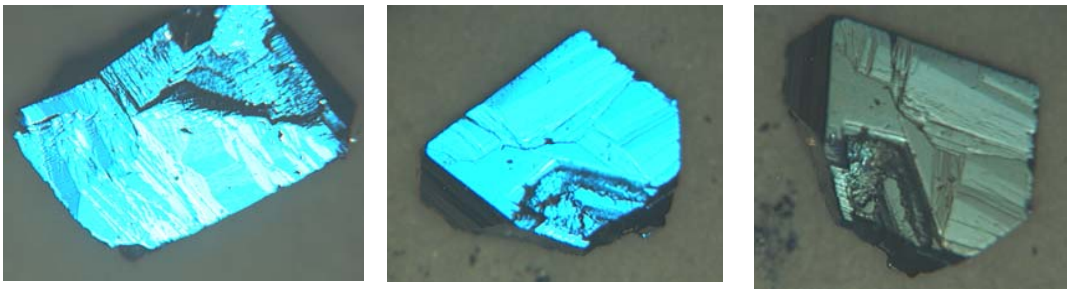

Figure 22. Microscope images of the cyclopropyl carbocyanine dye crystals. Middle and right pictures are of the same crystal at near right angle to each other under polarized light.

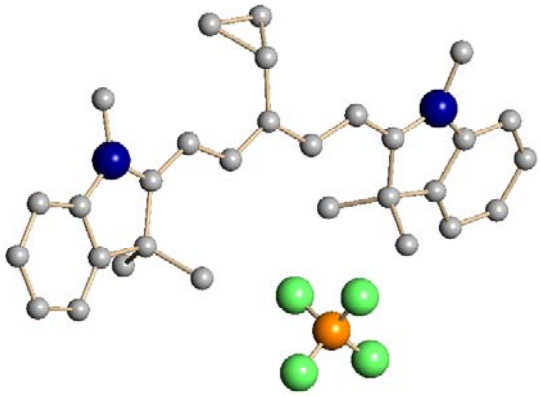

Figure 23. Crystal structure of cyclopropylcarbocyanine dye confirming the structure and tetrafluoroborate counterion.

These studies established our synthetic and processing capabilities to modify the carbocyanine structure and generate large, pure crystals for photonic studies. In addition to the molecular structure modification, exchange of the counterion could also lead to novel aggregate and crystalline packing structures.

V. Langmuir Films of Cyanine Dyes

Another route towards unique packing structures of cyanine dyes is the use of interfacial confinement to organize the dye molecules at high concentration with reduced degrees of freedom. One such structure is a Langmuir monolayer of amphiphilic molecules, which are confined at the air-water interface. Excellent examples of cyanine dyes in J-aggregate structure in Langmuir films can be found in the literature as existing at the air-water interface as well as transferred Langmuir-Blodgett (LB) films onto solid substrates.[41,42,43,44] Our goal here was to prepare large domains of J-aggregate cyanine dyes that would allow us to study the relationship between aggregate structure and size, as well as the molecular architecture, with its photonic behavior.

The initial efforts here concentrated on the preparation of Langmuir monolayers of cyanine dyes and the characterization of the resultant structures through fluorescence microscopy. The dye molecule, 3,3'-dioctadecyl oxacarbocyanine perchlorate (DiO) (Figure 24), was spread on the water surface from a chloroform/benzene solution. Pressure-area isotherm of the molecule shows a highly expanded phase that transforms to a solid phase at pressures above 35 mN/m (Figure 25). Two-dimensional crystals were observed within the film from low pressures, shown in Figure 26. Growth of the crystal size with increasing film pressure was not observed. Instead what was found was an abundance of smaller crystals formed as the pressure increased.

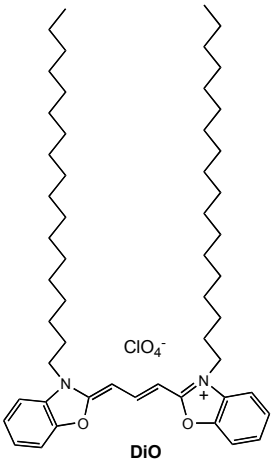

.

Figure 24. Molecular structure of DiO cyanine amphiphile

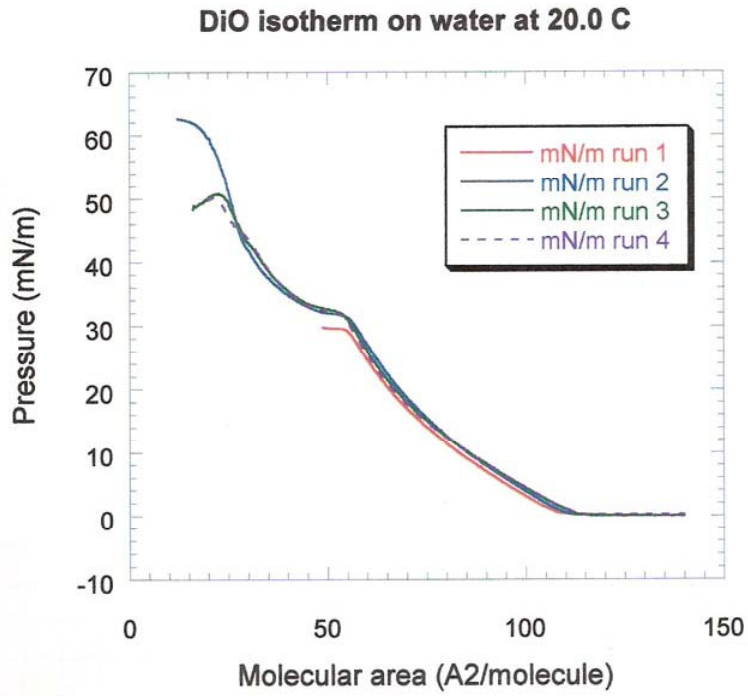

Figure 25. Langmuir isotherms of DiO on pure water. Multiple runs were performed to show the reproducibility of the pressure-area isotherm.

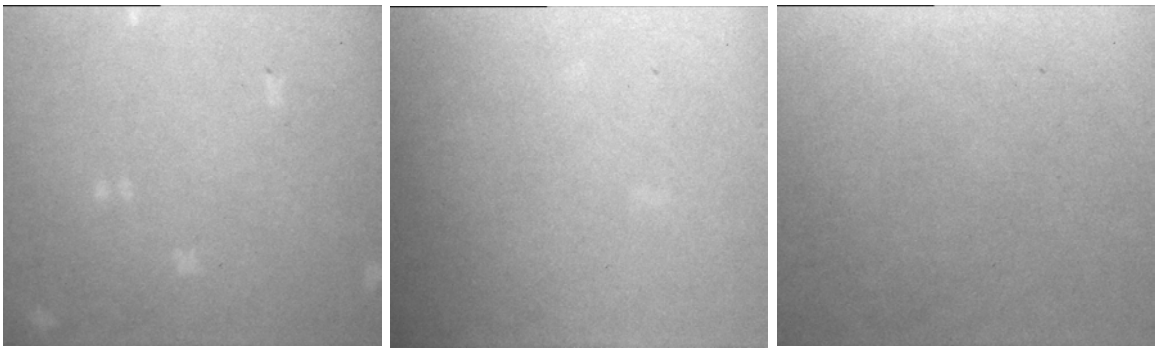

4 mN/m 10 mN/m 20 mN/m

Figure 26. Fluorescence microscopy images of DiO monolayer film at the air-water interface at various surface pressures. Large two-dimensional crystals of the cyanine dye can be seen as light rectangular structures at lower pressures but dissipate to smaller sizes at higher pressure.

Langmuir-Blodgett (LB) multilayer films of the DiO monolayer were transferred onto glass slides. The deposition was successfully performed at 40 mN/m producing a Y-type deposition where the headgroups and tailgroups of the amphiphiles align against each other yielding an alternating orientation of successively deposited monolayers. Interestingly, depositions run at lower surface pressure failed to obtain good monolayer transfer. On the left side of Figure 27 a plot of the molecular area with time during the deposition cycles is shown with the corresponding transfer ratio graph shown on the right side, performed at the surface pressure of 40 mN/m. The transfer ratio shows the amount of monolayer area transferred relative to the substrate area. A transfer ratio of 1 shows perfect transfer of the monolayer to match the substrate area. The plot in Figure 27 shows the deposition on the down stroke as the odd numbered strokes and the upstroke as the even numbered strokes. Deposition was poor on the first downstroke but near perfect on the next upstroke. The downstrokes after that improved towards 100%, whereas the upstokes gave near perfect transfer on all but the last stroke. The seven-layered film was a homogeneous yellow film with no observable defects.

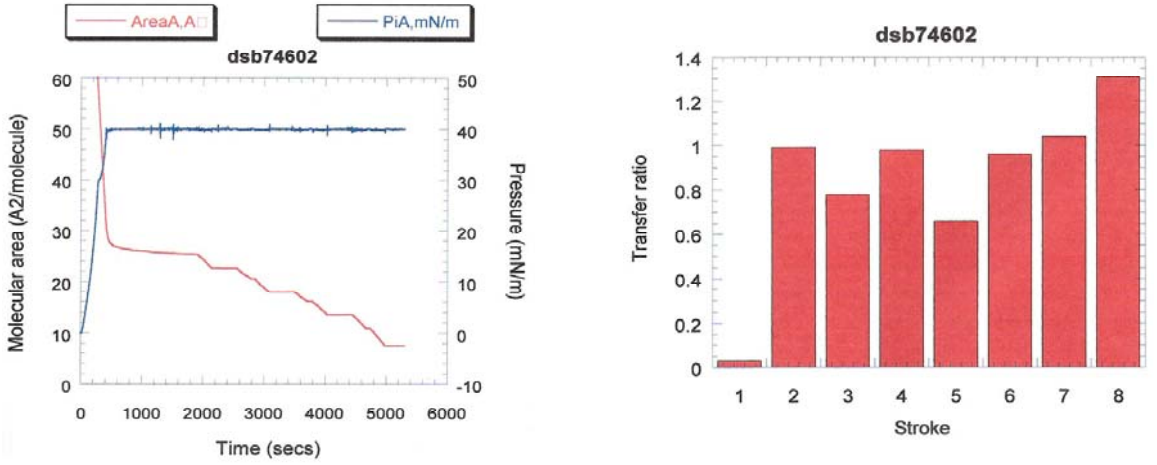

Figure 27. Langmuir-Blodgett deposition of DiO monolayers on glass slides at 40 mN/m, 20 °C (deposition rate 10 mm/min). Left – double Y-axis graph of molecular area and surface pressure vs. time (seconds). Right – transfer ratio of DiO monolayer onto glass slides.

Experimental

General. All compounds were of reagent grade purity and used as supplied by the manufacturer unless stated otherwise. Organic solvents were of reagent grade from Fisher Scientific. Aqueous solutions were prepared from water purified through a Barnstead Type D4700 NANOpure Analytical Deionization System with ORGANICfree cartridge registering an 18.0 MΩ-cm resistance. Fluorescence measurements were performed on a SPEX Fluoromax II spectrophotometer (Instruments SA, Edison, NJ) equipped with a jacketed cell. NMR analyses were performed on a Bruker DRX 400 (Billerica, MA) with a resonance frequency of 400.1 MHz for ^{1}H and 100.6 MHz for ^{13}C. Elemental analyses were performed by Desert Analytics (Tucson, AZ).

1-cyclopropyl-2-methoxy-ethylene

Methoxymethyl-triphenylphosphonium chloride (48 mmole, 16.45 g) was suspended in anhydrous diethyl ether (200 mL), in a 500 mL schlenk flask under nitrogen. Butyl lithium (48 mmole at 2M in THF) was added slowly. The reaction mixture was cooled to -41 °C, and cyclopropylcarboxaldehyde (40 mmole, 3.0 mL) was added. The reaction was stirred at -41 °C for 30 min then allowed to reach room temperature and stirred over night. Non-acid washed Celite (20 mL) was added and the reaction mixture was filtered. The precipitate was washed with petroleum ether (2 x 50 mL). Basic alumina (20 mL) was stirred into the combined filtrate and then removed by vacuum filtration. Cis and trans 1-cyclopropyl-2-methoxy-ethylene were isolated by distillation at 70 °C to 112 °C. ^{1}H NMR ($CDCl_3$) found cyclopropyl protons (multiplets) at 0.26, 0.6, and 0.85 ppm, methoxy singlets at 3. 48 and 3.62, and olefinic protons (doublets) centered at 5.91 and 6.38 ppm and doublet of doublets at 3.87 and 4.48 ppm. This fraction (26 mL) was taken on to the next step without further purification.

2-cyclopropyl-3-(N,N-dimethylamino)prop-2-ene-1-aldehyde

1-cycloproyl-2-methoxy-ethylene (~ 40 mmole) was combined with potassium carbonate (80 mmole, 11 g) and Vilsmeier reagent (60 mmole, 7.7 g) in dichloroethane (50 mL) and the mixture heated to reflux with stirring over night. After the mixture was cooled to room temperature the supernatant was decanted, diluted to 150 mL with chloroform and washed with 10% aq. NaOH, followed by water and then brine. The product was purified by chromatography on 100 mL silica gel pre-treated with 2% triethylamine in hexane. Elution was done in a gradient using 1:1 hexanes-chloroform with 2 % trietylamine first followed by 99.5% cloroform-0.5 % triethylamine, and then finally 100% chloroform. 2-cyclopropyl-3-(N,N-dimethylamino)pop-2-ene-1-aldehyde (6.5 mmole, 900 mg) was isolated in 16% yield. The structure was confirmed by ^{1}H NMR ($CDCl_3$) [peaks at 8.84, 8.57, 3.35, 1.36, 0.848, and 0.491 ppm].

2-cyclopropyl malonaldehyde

2-cyclopropyl-3-(N,N-dimethylamino)prop-2-ene-1-aldehyde (6.5 mmole, 900 mg) was suspended in 10% aq. sodium hydroxide (5.2 mL) and heated to 70°C for 30 min. The reaction mixture was allowed to cool to room temperature, then 16 mL of 1N HCL was added. The solution was extracted with dichloromethane (3 x 20 mL), the organics combined and concentrated under reduced pressure. The product 2-cyclopropyl malonaldehyde (4.11 mmole,

460 mg) was collected in 63% yield. The structure was confirmed by ^{1}H NMR ($CDCl_3$) [peaks at 8.35, 1.47, 0.76, and 0.37 ppm].

χ-cyclopropyl-1,3,3,1',3',3'-hexamethyl indocarbocyanine tetrafluoroborate

2-cyclopropylmalonaldehyde (4.11 mmole, 460 mg) was combined with acetic anhydride (20 mL) and sodium acetate (8.5 mmole, 700 mg) and to the mixture was added tetramethylindolinium iodide (8.21 mmole, 2.47 g) was added as a solid. The reaction was stirred under nitrogen at 80 °C for 1 hr, followed by heating to 90 °C for 1 hr. The solution was then allowed to cool to room temperature and continued stirring for 3h. The solvents were removed by distillation under vacuum and the remaining residue precipitated from diethyl ether at -10 °C to yield 1.23g of a crude purple solid.

The product was further purified by ion pairing chromatography on 100 mL of silica that had been treated with 400 mL of 5% NaI in acetone followed by vacuum filtration and drying at 35°C, 4 mm Hg. Elution was performed with a gradient of chloroform to 10% methanol/chloroform, saturated with sodium iodide. Fractions containing the product were combined, dried under vacuum, re-dissolved in chloroform, and then filtered through a 0.45 micron PTFE filter. The solution was evaporated and re-dissolved in hot methanol (20 mL) and 10 % aq $NaBF_4$ (50 mL) was added slowly while vortexing. The solution was then cooled and filtered. This process was repeated twice. Further purification was achieved by recrystallization from isopropanol to yield pure χ-cyclopropyl-1,3,3,1',3',3'-hexamethyl indocarbocyanine tetrafluoroborate (0.78 mmole, 400 mg) in 19% yield. ^{1}H NMR ($CDCl_3$) δ 8.018 - 7.983 (d, J = 14 Hz, 2H, olefinic), 7.395 - 7.360 (m, 4H, aromatic), 7.263 - 7.212 (m, 2.7H, aromatic and $CHCl_3$), 7.159 - 7.138 (d, J = 8.4 Hz, 2H, aromatic), 6.511 - 6.476 (d, J = 14 Hz, 2H, olefinic), 3.682 (s, 6H, 1 and 1' methyl), 1.723 (s, 12H, 3 and 3' geminal dimethyls), 1.492 (m, 1H, cyclopropyl methyne), 1.154 - 1.136 (d, J = 7.2 Hz, 2H, cyclopropyl methylene), 0.545 - 0.507 (m, 2H, cyclopropyl methylene). X-ray diffraction: see attached data.

X-ray crystal structure determination

A dark blue crystal was mounted on a thin glass fiber using fluorolube. The crystal, which was mounted from a pool of fluorolube, was then immediately placed under a liquid N_2 stream on a Bruker AXS diffractometer. The radiation used was graphite monochromatized Mo Kα radiation (λ=0.71073 A). The lattice parameters were optimized from a least-squares calculation on ~200 centered reflections. Lattice determination and data collection were carried out using SMART Ver. 5.626 software. Data reduction was performed using SAINT+ 6.22 software. Structure solution was performed using SHELXTL Ver. 6.10 (12/05/00) software. The structure refinement was performed using XSHELL Ver. 4.02 (12/05/2000) software. The data was corrected for absorption using the program SADABS (Ver. 2.03) within the SAINT+ package. Data collection parameters are given in Table 1.

The structure was solved in the space group P-1 using Direct Methods. This solution yielded entire molecule with its expected structure. The hydrogen atoms were fixed in positions of ideal geometry and refined within the XSHELL software. These idealized hydrogen atoms had their isotropic temperature parameters fixed at 1.2 or 1.5 times the equivalent isotropic temperature parameter (U) of the C atoms for which they were bonded. The final refinement included anisotropic thermal parameters on all non-hydrogen atoms and converged to R1=0.0813 and R2w=0.1315.

Table 1. Crystal data and structure refinement for cycloPr-hexaM-pentamethyncyanine-BF4.

Identification code	mar093s
Empirical formula	C30 H35 B F4 N2
Formula weight	510.41
Temperature	168(2) K
Wavelength	0.71073 A
Crystal system, space group	Triclinic, P-1
Unit cell dimensions	a = 9.7592(17) A alpha = 92.508(3) deg. b = 10.9686(18) A beta = 100.853(3) deg. c = 13.146(2) A gamma = 104.770(3) deg.
Volume	1330.2(4) A^3
Z, Calculated density	2, 1.274 Mg/m^3
Absorption coefficient	0.093 mm^-1
F(000)	540
Crystal size	0.20 x 0.05 x 0.00 mm
Theta range for data collection	1.93 to 23.28 deg.
Limiting indices	-10<=h<=10, -12<=k<=11, -14<=l<=14
Reflections collected / unique	6808 / 3723 [R(int) = 0.0619]
Completeness to theta = 23.28	97.3 %
Absorption correction	SADABS
Refinement method	Full-matrix least-squares on F^2
Data / restraints / parameters	3723 / 0 / 340
Goodness-of-fit on F^2	1.039
Final R indices [I>2sigma(I)]	R1 = 0.0813, wR2 = 0.1315
R indices (all data)	R1 = 0.1449, wR2 = 0.1538
Largest diff. peak and hole	0.360 and -0.212 e.A^-3

Table 2. Atomic coordinates (x 10^4) and equivalent isotropic displacement parameters (A^2 x 10^3) for cycloPr-hexaM-pentamethyncyanine-BF4. U(eq) is defined as one third of the trace of the orthogonalized Uij tensor.

	x	y	z	U(eq)
B(1)	3859(8)	7381(6)	3579(5)	39(2)
F(1)	5063(4)	6995(4)	3597(3)	106(2)
F(2)	2687(3)	6483(3)	2957(2)	49(1)
F(3)	3985(4)	8524(3)	3187(3)	77(1)
F(4)	3579(4)	7510(3)	4569(2)	65(1)
N(1)	3387(4)	5570(4)	-1582(3)	23(1)
N(2)	2106(4)	1355(3)	4673(3)	23(1)
C(1)	2596(5)	3196(4)	1389(3)	23(1)
C(2)	2787(5)	2029(4)	886(3)	23(1)
C(3)	1826(5)	1431(4)	-149(4)	30(1)
C(4)	1657(6)	788(5)	809(4)	37(1)
C(5)	2645(5)	4278(4)	884(4)	23(1)
C(6)	2974(5)	4444(4)	-108(3)	21(1)
C(7)	3073(5)	5520(4)	-614(4)	23(1)
C(8)	3642(5)	4534(4)	-2185(3)	29(1)
C(9)	3512(5)	6796(4)	-1924(4)	23(1)
C(10)	3889(5)	7235(5)	-2829(4)	27(1)
C(11)	4043(5)	8520(5)	-2937(4)	30(1)
C(12)	3837(5)	9300(5)	-2169(4)	33(1)
C(13)	3421(5)	8828(5)	-1279(4)	31(1)
C(14)	3261(5)	7562(4)	-1157(4)	23(1)
C(15)	2922(5)	6816(4)	-265(3)	23(1)
C(16)	1336(5)	6709(5)	-160(4)	39(2)
C(17)	3971(5)	7436(4)	745(3)	31(1)
C(18)	2349(5)	3216(4)	2412(4)	24(1)
C(19)	2390(5)	2270(4)	3071(3)	21(1)
C(20)	1974(5)	2258(4)	4031(4)	21(1)
C(21)	2871(5)	376(4)	4570(4)	34(1)
C(22)	1446(5)	1477(4)	5528(3)	23(1)
C(23)	1308(5)	688(5)	6321(4)	30(1)
C(24)	561(6)	996(5)	7047(4)	40(2)
C(25)	-27(6)	2012(5)	6978(4)	41(2)
C(26)	112(6)	2781(5)	6165(4)	36(1)
C(27)	883(5)	2509(4)	5439(3)	22(1)
C(28)	1250(5)	3155(4)	4501(4)	22(1)
C(29)	-113(5)	3286(5)	3769(4)	32(1)
C(30)	2368(5)	4441(4)	4863(4)	33(1)

Table 3. Bond lengths [A] and angles [deg] for cycloPr-hexaM-pentamethyncyanine-BF4.

B(1)-F(1)	1.343(7)
B(1)-F(3)	1.362(7)
B(1)-F(4)	1.388(7)
B(1)-F(2)	1.396(7)
N(1)-C(7)	1.364(5)
N(1)-C(9)	1.420(6)
N(1)-C(8)	1.456(5)
N(2)-C(20)	1.345(5)
N(2)-C(22)	1.415(5)
N(2)-C(21)	1.470(5)
C(1)-C(5)	1.381(6)
C(1)-C(18)	1.409(6)
C(1)-C(2)	1.485(6)
C(2)-C(4)	1.503(6)
C(2)-C(3)	1.513(6)
C(3)-C(4)	1.486(6)
C(5)-C(6)	1.409(6)
C(6)-C(7)	1.371(6)
C(7)-C(15)	1.525(6)
C(9)-C(14)	1.381(6)
C(9)-C(10)	1.381(6)
C(10)-C(11)	1.395(6)
C(11)-C(12)	1.371(6)
C(12)-C(13)	1.387(7)
C(13)-C(14)	1.377(6)
C(14)-C(15)	1.498(6)
C(15)-C(17)	1.527(6)
C(15)-C(16)	1.556(6)
C(18)-C(19)	1.385(6)
C(19)-C(20)	1.396(6)
C(20)-C(28)	1.521(6)
C(22)-C(27)	1.380(6)
C(22)-C(23)	1.387(6)
C(23)-C(24)	1.384(6)
C(24)-C(25)	1.376(7)
C(25)-C(26)	1.396(7)
C(26)-C(27)	1.387(6)
C(27)-C(28)	1.505(6)
C(28)-C(29)	1.531(6)
C(28)-C(30)	1.538(6)
F(1)-B(1)-F(3)	111.1(6)
F(1)-B(1)-F(4)	111.5(6)

F(3)-B(1)-F(4)	107.5(5)
F(1)-B(1)-F(2)	108.8(5)
F(3)-B(1)-F(2)	109.3(5)
F(4)-B(1)-F(2)	108.6(5)
C(7)-N(1)-C(9)	111.4(4)
C(7)-N(1)-C(8)	125.5(4)
C(9)-N(1)-C(8)	123.0(4)
C(20)-N(2)-C(22)	111.1(4)
C(20)-N(2)-C(21)	126.9(4)
C(22)-N(2)-C(21)	121.9(4)
C(5)-C(1)-C(18)	118.1(4)
C(5)-C(1)-C(2)	121.9(4)
C(18)-C(1)-C(2)	119.9(4)
C(1)-C(2)-C(4)	120.4(4)
C(1)-C(2)-C(3)	120.1(4)
C(4)-C(2)-C(3)	59.0(3)
C(4)-C(3)-C(2)	60.2(3)
C(3)-C(4)-C(2)	60.8(3)
C(1)-C(5)-C(6)	125.3(4)
C(7)-C(6)-C(5)	126.4(4)
N(1)-C(7)-C(6)	121.4(4)
N(1)-C(7)-C(15)	108.0(4)
C(6)-C(7)-C(15)	130.6(4)
C(14)-C(9)-C(10)	122.9(4)
C(14)-C(9)-N(1)	108.4(4)
C(10)-C(9)-N(1)	128.7(4)
C(9)-C(10)-C(11)	116.9(5)
C(12)-C(11)-C(10)	120.8(5)
C(11)-C(12)-C(13)	121.1(5)
C(14)-C(13)-C(12)	119.0(5)
C(13)-C(14)-C(9)	119.2(5)
C(13)-C(14)-C(15)	130.8(4)
C(9)-C(14)-C(15)	109.9(4)
C(14)-C(15)-C(7)	102.2(4)
C(14)-C(15)-C(17)	110.5(4)
C(7)-C(15)-C(17)	113.6(4)
C(14)-C(15)-C(16)	110.0(4)
C(7)-C(15)-C(16)	110.0(4)
C(17)-C(15)-C(16)	110.1(4)
C(19)-C(18)-C(1)	126.4(4)
C(18)-C(19)-C(20)	124.6(4)
N(2)-C(20)-C(19)	122.7(4)
N(2)-C(20)-C(28)	109.0(4)
C(19)-C(20)-C(28)	128.2(4)
C(27)-C(22)-C(23)	123.7(4)
C(27)-C(22)-N(2)	108.7(4)

C(23)-C(22)-N(2)	127.6(4)
C(24)-C(23)-C(22)	115.9(5)
C(25)-C(24)-C(23)	122.0(5)
C(24)-C(25)-C(26)	120.9(5)
C(27)-C(26)-C(25)	118.2(5)
C(22)-C(27)-C(26)	119.2(5)
C(22)-C(27)-C(28)	109.4(4)
C(26)-C(27)-C(28)	131.3(4)
C(27)-C(28)-C(20)	101.4(4)
C(27)-C(28)-C(29)	111.2(4)
C(20)-C(28)-C(29)	113.1(4)
C(27)-C(28)-C(30)	109.1(4)
C(20)-C(28)-C(30)	109.2(4)
C(29)-C(28)-C(30)	112.3(4)

Symmetry transformations used to generate equivalent atoms:

Table 4. Anisotropic displacement parameters (A^2 x 10^3) for cycloPr-hexaM-pentamethyncyanine-BF4.

The anisotropic displacement factor exponent takes the form:
-2 pi^2 [h^2 a*^2 U11 + ... + 2 h k a* b* U12]

	U11	U22	U33	U23	U13	U12
B(1)	49(5)	26(4)	38(4)	-5(3)	12(4)	2(4)
F(1)	62(3)	124(4)	133(4)	-54(3)	-4(3)	54(3)
F(2)	65(2)	33(2)	40(2)	-3(2)	9(2)	-2(2)
F(3)	121(4)	30(2)	82(3)	9(2)	53(3)	1(2)
F(4)	90(3)	57(2)	42(2)	-9(2)	22(2)	8(2)
N(1)	29(3)	21(2)	23(2)	4(2)	8(2)	10(2)
N(2)	24(2)	20(2)	26(2)	3(2)	2(2)	9(2)
C(1)	21(3)	21(3)	26(3)	-2(2)	3(2)	7(2)
C(2)	21(3)	17(3)	30(3)	-2(2)	4(2)	5(2)
C(3)	31(3)	31(3)	26(3)	-3(3)	2(3)	10(3)
C(4)	44(4)	25(3)	39(3)	-2(3)	11(3)	1(3)
C(5)	24(3)	18(3)	30(3)	-1(2)	8(2)	10(2)
C(6)	26(3)	18(3)	21(3)	-2(2)	5(2)	9(2)
C(7)	19(3)	23(3)	26(3)	2(2)	0(2)	9(2)
C(8)	37(3)	26(3)	23(3)	-2(2)	4(2)	7(3)
C(9)	18(3)	26(3)	24(3)	5(2)	1(2)	7(2)
C(10)	24(3)	30(3)	22(3)	0(2)	0(2)	4(3)
C(11)	23(3)	37(4)	29(3)	16(3)	1(2)	5(3)
C(12)	35(3)	24(3)	40(3)	8(3)	5(3)	9(3)
C(13)	30(3)	31(3)	34(3)	-2(3)	6(3)	15(3)
C(14)	23(3)	21(3)	27(3)	1(2)	5(2)	10(2)
C(15)	23(3)	19(3)	26(3)	0(2)	4(2)	8(2)
C(16)	31(3)	37(4)	56(4)	13(3)	20(3)	13(3)
C(17)	43(4)	20(3)	29(3)	4(2)	10(3)	7(3)
C(18)	22(3)	23(3)	29(3)	1(2)	9(2)	7(2)
C(19)	23(3)	20(3)	23(3)	2(2)	6(2)	9(2)
C(20)	16(3)	17(3)	27(3)	2(2)	-4(2)	4(2)
C(21)	37(3)	25(3)	40(3)	4(3)	2(3)	15(3)
C(22)	18(3)	30(3)	16(3)	1(2)	2(2)	0(2)
C(23)	27(3)	33(3)	25(3)	8(3)	2(3)	4(3)
C(24)	40(4)	43(4)	27(3)	11(3)	5(3)	-5(3)
C(25)	38(4)	53(4)	30(3)	3(3)	13(3)	4(3)
C(26)	32(3)	45(4)	32(3)	-2(3)	8(3)	12(3)
C(27)	17(3)	30(3)	20(3)	2(2)	3(2)	7(2)
C(28)	22(3)	21(3)	27(3)	4(2)	5(2)	11(2)
C(29)	30(3)	37(3)	36(3)	8(3)	9(3)	19(3)
C(30)	40(3)	28(3)	29(3)	-3(3)	7(3)	5(3)

Table 5. Hydrogen coordinates (x 10^4) and isotropic displacement parameters (A^2 x 10^3) for cycloPr-hexaM-pentamethyncyanine-BF4.

	x	y	z	U(eq)
H(2)	3808	1969	989	27
H(3A)	1061	1829	-458	36
H(3B)	2269	1056	-658	36
H(4A)	1993	13	892	45
H(4B)	786	785	1092	45
H(5)	2441	4967	1233	28
H(6)	3144	3740	-462	25
H(8A)	4413	4231	-1772	44
H(8B)	3934	4835	-2824	44
H(8C)	2752	3840	-2365	44
H(10)	4036	6687	-3354	32
H(11)	4293	8859	-3551	36
H(12)	3982	10177	-2247	40
H(13)	3250	9371	-762	37
H(16A)	1204	7559	-63	59
H(16B)	1136	6248	441	59
H(16C)	668	6251	-793	59
H(17A)	4968	7514	666	46
H(17B)	3767	6913	1313	46
H(17C)	3852	8279	906	46
H(18)	2134	3951	2674	29
H(19)	2724	1580	2855	25
H(21A)	3128	368	3885	50
H(21B)	2241	-454	4643	50
H(21C)	3753	562	5114	50
H(23)	1702	-20	6364	36
H(24)	452	491	7611	48
H(25)	-535	2192	7491	49
H(26)	-311	3472	6110	44
H(29A)	-727	2444	3477	48
H(29B)	164	3785	3204	48
H(29C)	-648	3715	4158	48
H(30A)	1951	4977	5261	50
H(30B)	2628	4856	4255	50
H(30C)	3236	4308	5303	50

Langmuir Film Studies

The dye molecule 3,3'-dioctadecyl oxacarbocyanine perchlorate (Molecular Probes, Inc., Eugene, OR) was used as received. Pressure-area (π-A) isotherms and Langmuir-Blodgett film preparations were performed on a Nima 2011 circular Langmuir trough (Coventry, England). The trough was situated on a vibration isolation table inside a class 100 clean room. The pure water subphase was kept at a temperature of 20 ± 0.2 ^{o}C. The dye amphiphiles were spread on the water surface in a 50% chloroform/benzene solution. All films were incubated for 10 – 15 minutes at zero pressure prior to compression. The compression rate for the π-A isotherms and for LB preparation was 100 cm^2/min (4 Å^2/molecule•min). For LB deposition cleaned glass slides were stroked through the monolayer at a rate of 10 mm/min with a pause time of 30 seconds at the bottom of the stroke and a rest time of 10 minutes between down-up cycles.

References

[1] V. A. Shchukin and D. Bimberg, "Spontaneous ordering of nanostructures on crystal surfaces", Rev. Mod. Phys. **71**, 1125 (1999).

[2] N. N. Ledentsov, V. A. Shchukin, M. Grundmann, N. Kirstaedter, J. Böhrer, O. Schmidt, D. Bimberg, V. M. Ustinov, A. Yu. Egorov, A. E. Zhukov, P. S. Kop'ev, S. V. Zaitsev, N. Yu. Gordeev, Zh. I. Alferov, A. I. Borovkov, A. O. Kosogov, S. S. Ruvimov, P. Werner, U. Gösele, and J. Heydenreich, "Direct formation of vertically coupled quantum dots in Stranski-Krastanow growth", Phys. Rev. B **54**, 8743 (1996).

[3] Z. Gai, B. Wu, J. P. Pierce, G. A. Farnan, D. Shu, M. Wang, Z. Zhang, and J. Shen, "Self-assembly of nanometer-scale magnetic dots with narrow size distributions on an insulating substrate", Phys. Rev. Lett. **89**, 235502 (2002).

[4] J. A. Floro, G. A. Lucadamo, E. Chason, L. B. Freund, M. Sinclair, R. D. Twesten, and R. Q. Hwang, "SiGe island shape transitions induced by elastic repulsion", Phys. Rev. Lett. **80**, 4717 (1998).

[5] Z. Gai, G. A. Farnan, J. P. Pierce, and J. Shen, "Growth of low-dimensional magnetic nanostructures on an insulator", Appl. Phys. Lett. **81**, 742 (2002).

[6] M. P. Zach, K. H. Ng, R. M. Penner, "Molybdenum nanowires by electrodeposition", Science **290**, 2120 (2000).

[7] S. Morin, A. Lachenwitzer, O. M. Magnussen, and R. J. Behm, "Potential-controlled step flow to 3D step decoration transition: Ni electrodeposition on Ag(111)", Phys. Rev. Lett. **83**, 5066 (1999).

[8] C. Yu, D. Li, J. Pearson, and S. D. Bader, "Alignment of self-assembled magnetic nanostructures: Co dot chains and stripes on grooved Ru(0001)", Appl. Phys. Lett. **79**, 3848 (2001).

[9] Y.-N. Yang, E. S. Fu, and E. D. Williams, "An STM study of current-induced step bunching on Si(111)", Surf. Sci. **356**, 101 (1996).

[10] J. Kuntze, A. Mugarza, and J. E. Ortega, "Ag-induced zero- and one-dimensional nanostrucutures on vicinal Si(111)", Appl. Phys. Lett. **81**, 2463 (2002).

[11] S. A. Maier, P. G. Kik, and H. A. Atwater, "Optical pulse propogation in metal nanoparticle chain waveguides", Phys. Rev. B **67**, 205402 (2003).

[12] S. S. Perry and P. B. Merrill, "Preparation and characterization of MgO(100) surfaces", Surf. Sci. **383**, 268 (1997).

[13] S. S. Perry, H. I. Kim, S. Imaduddin, S. M. Lee, and P. B. Merrill, "Generation of atomically flat MgO(100) surfaces: Influence of ambient gas composition during high temperature anneals", J. Vac. Sci. Technol. A **16**, 3402 (1998).

[14] M. P. Delplancke-Ogletree, M. Ye, and R. Winand, "Influence of thermal annealing and humidity exposure on surface structure of (100) single-crystal MgO substrate", J. Mater. Res. **14**, 2133 (1999).

[15] O. Robach, G. Renaud, and A. Barbier, "Structure and morphology of the Ag/MgO(001) interface during in situ growth at room temperature", Phys. Rev. B **60**, 5858 (1999).

[16] J. B. Pendry, "Playing tricks with light", Science **285**, 1687 (1999).

[17] J. R. Sambles, "More than transparent", Nature (London) **391**, 641 (1998).

[18] T. W. Ebbesen, H. J. Lezec, H. F. Ghaemi, T. Thio, and P. A. Wolff, "Extraordinary optical transmission through sub-wavelength hole arrays", Nature **391**, 667 (1998).

[19] M. Fleischmann, P. Hendra, and A. J. McQuillan, "Raman spectra of pyridine adsorbed at a silver electrode", Chem. Phys. Lett. **26**, 163 (1974).

[20] W. R. Holland and D. G. Hall, "Surface-plasmon dispersion relation: Shifts induced by the interaction with localized plasmon resonances", Phys. Rev. B **27**, 7765 (1983).

[21] A. Leitner, Z. Zhao, H. Brunner, F. R. Aussenegg, and A. Wokaun, "Optical properties of a metal island film close to a smooth metal surface", Appl. Optics **32**, 102 (1993).

[22] H. R. Stuart and D. G. Hall, "Enhanced dipole-dipole interaction between elementary radiators near a surface", Phys. Rev. Lett. **80**, 5663 (1998).

[23] A. K. Sarychev, V. A. Shubin, and V. M. Shalaev, "Percolation-enhanced nonlinear scattering from metal-dielectric composites", Phys. Rev. E **59**, 7239 (1999).

[24] J. A. Floro, E. Chason, S. R. Lee, R. D. Twesten, and R. Q. Hwang, "Real-time stress evolution during $Si_{1-x}Ge_x$ Heteroepitaxy: Dislocations, Islanding, and Segregation", Electron. Mater. **26**, 983 (1997).

[25] R. Koch, "The intrinsic stress of polycrystalline and epitaxial thin metal films", J. Phys.: Condens. Matter **6**, 9519 (1994).

[26] J. A. Floro, E. Chason, R. C. Cammarata, and D. J. Srolovitz, "Physical origins of intrinsic stress in Volmer-Weber thin films", MRS Bull. **28**, 19 (2002).

[27] J. A. Floro, P. G. Kotula, S. C. Seel, and D. J. Srolovitz, "Origins of growth stresses in amorphous semiconductor thin films", Phys. Rev. Lett. **91**, 096101 (2003).

[28] S. C. Seel, C. V. Thompson, S. J. Hearne, and J. A. Floro, "Tensile stress evolution during deposition of Volmer-Weber thin films", J. Appl. Phys. **88**, 7079 (2000).

[29] M. Born and E. Wolf, *Principles of Optics*, 6th ed., Permagon, 1980.

[30] *Handbook of Optical Constants of Solids*, edited by E. D. Palik, Academic, 1985.

[31] G. A. N Connell, R. J. Temkin, and W. Paul, "Amorphous germanium III. Optical properties", Adv. Phys. **22**, 643 (1974).

[32] C. F. Bohren and D. R. Huffman, *Absorption and Scattering of Light by Small Particles*, Wiley-Interscience, 1983.

[33] W. C. Sweatt, S. A. Kemme, and M. E. Warren, "Diffractive Optical Elements", SAND2002-2543P (2002).

[34] M. H. Brodsky, R. S. Title, K. Weiser, and G. D. Pettit, "Structural, optical, and electrical properties of amorphous silicon films", Phys. Rev. B **1**, 2632 (1970).

[35] H. R. Stuart and D. G. Hall, "Absorption enhancement in silicon-on-insulator waveguides using metal island films", App. Phys. Lett. **69**, 2327 (1996).

[36] H. R. Stuart and D. G. Hall, "Island size effects in nanoparticle-enhanced photodetectors", Appl. Phys. Lett. **73**, 3815 (1998).

[37] Mishra A, Behera RK, Behera PK, Mishra BK, Behera GB. 2000. Cyanines during the 1990's: A Review. Chem. Rev. 100(6):1973 - 2001.

[38] Kuhn H, Kuhn C. 1996. Chromophore coupling effects. In: Kobayashi T, editor. J-Aggregates. Singapore: World Scientific. p 1 - 40.

[39] Allmann R, Debaerdemaeker T, Ferwanah A-R, Pressler W, Reichardt C. 1976. g-Cycloalkyl-pentamethincyanin-Farbstoffe. Chem. Ber. 109:3005 - 3016.

[40] Ferwanah A, Pressler W, Reichardt C. 1973. Synthese und eigenschaften von cycloalkyl-malondialdehyden. Tet. Lett. 40:3979 - 3982.

[41] Watanabe T, Asai K, Ishigure K. 1998. Control of domain structure of a cyanine dye Langmuir-Blodgett film. Thin Solid Films 322:188 - 193.

[42] von Berlepsch H, Böttcher C, Ouart A, Regenbrecht M, Akari S, Keiderling U, Schnablegger H, Dähne S, Kirstein S. 2000. Surfactant-Induced Changes of Morphology of J-Aggregates: Superhelix-to-Tubule Transformation. Langmuir 16:5908 - 5916.

[43] Lehmann U. 1988. Aggregation of cyanine dyes at Langmuir-Blodgett monolayers. Thin Solid Films 160:257 - 269.

[44] Penner TL. 1988. J-aggregates of dyes in Langmuir-Blodgett films. J. Chimie Phys. Phys.-Chimie Biol. 85(11 - 12):1081 - 1084.

DISTRIBUTION:

1	MS 1411	M. Sinclair
1	MS 1413	D. Sasaki
1	MS 1415	J. Floro
1	MS 1415	S. Seel
1	MS 1415	T.A. Westrich
1	MS 0123	D.L. Chavez, LDRD Office
1	MS 9018	Central Technical Files, 8945-1
2	MS 0899	Technical Library, 9616